A&A 501, 221–237 (2009)
DOI: 10.1051/0004-6361/200810960

Astronomy & Astrophysics

CO emission and variable CH and CH^+ absorption towards HD 34078: evidence for a nascent bow shock?*

P. Boissé[1], E. Rollinde[2], P. Hily-Blant[3], J. Pety[4], S. R. Federman[5], Y. Sheffer[5], G. Pineau des Forêts[6], E. Roueff[7], B.-G. Andersson[8], and G. Hébrard[2]

[1] Institut d'Astrophysique de Paris (IAP), UMR7095 CNRS, Université Pierre et Marie Curie-Paris6, 98 bis boulevard Arago, 75014 Paris, France
e-mail: boisse@iap.fr
[2] Institut d'Astrophysique de Paris, UMR7095 CNRS, Université Pierre et Marie Curie-Paris6, 98 bis boulevard Arago, 75014 Paris, France
[3] IRAM, Domaine Universitaire, 300 rue de la Piscine, 38406 Saint-Martin-d'Hères; Laboratoire d'Astrophysique, Observatoire de Grenoble, BP 53, 38041 Grenoble Cedex 9, France
[4] Institut de Radioastronomie Millimétrique, 300 rue de la Piscine, 38406 Saint Martin d'Hères; Observatoire de Paris, 61 Av. de l'Observatoire, 75014 Paris, France
[5] Department of Physics and Astronomy, University of Toledo, Toledo, OH 43606, USA
[6] IAS, Université d'Orsay, 91405 Orsay Cedex, France
[7] LUTH, Observatoire de Paris-Meudon, 92195 Meudon Cedex, France
[8] NASA Ames Research Center, Moffett Field, CA 94035, USA

Received 11 September 2008 / Accepted 24 January 2009

ABSTRACT

Context. The runaway star HD 34078, initially selected to investigate small scale structure in a foreground diffuse cloud, has been shown to be surrounded by highly excited H_2, the origin of which is unclear.

Aims. We first search for an association between the foreground cloud and HD 34078. Second, we extend previous investigations of temporal absorption line variations (CH, CH^+, H_2) in order to better characterize them and understand their relation to small-scale structure in the molecular gas.

Methods. We have mapped the ^{12}CO(2–1) emission at 12″ resolution around HD 34078's position, using the 30 m IRAM antenna. The follow-up of CH and CH^+ absorption lines has been extended over 5 more years: 26 visible spectra have been acquired since 2003 at high or intermediate resolution. In parallel, CH absorption towards the reddened star ζ Per has been monitored to check the instrumental stability and homogeneity of our measurements. Three more FUSE spectra have been obtained to search for $N(H_2)$ variations.

Results. CO observations show a pronounced maximum near HD 34078's position, clearly indicating that the star and diffuse cloud are associated. The optical spectra confirm the reality of strong, rapid and correlated CH and CH^+ fluctuations (up to 26% for $N(CH^+)$ between 2007 and 2008). On the other hand, $N(H_2, J = 0)$ has varied by less than 5% over 4 years, indicating the absence of marked density structure at scales below 100 AU. We also discard N(CH) variations towards ζ Per at scales less than 20 AU.

Conclusions. Observational constraints from this work and from 24 μm dust emission appear to be consistent with H_2 excitation but inconsistent with steady-state bow shock models and rather suggest that the shell of compressed gas surrounding HD 34078 or lying at the boundary of a small foreground clump is seen at an early stage of the interaction. The CH and CH^+ time variations as well as their high abundances are likely due to chemical structure in the shocked gas layer located at the stellar wind/ambient cloud interface. Finally, the lack of variation in both $N(H_2, J = 0)$ towards HD 34078 and N(CH) towards ζ Per suggests that quiescent molecular gas is not subject to pronounced small-scale structure.

Key words. ISM: molecules – stars: individual: HD 34078 – ISM: structure – ISM: individual objects: HD 34078

1. Introduction

During the past decade strong evidence has accumulated indicating that the spatial distribution of species like Na I and Ca II within neutral interstellar (IS) gas displays significant structure at AU scales (Crawford 2003; Lauroesch 2007; Welty 2007; Welty et al. 2008). H I itself, within the cold neutral medium at least, shows such structure (Frail et al. 1994; Heiles 1997; Deshpande 2007; Weisberg & Stanimirović 2007). In diffuse molecular gas, similar conclusions have been reached for tracers like H_2CO, HCO^+, and OH (Moore & Marscher 1995; Liszt & Lucas 2000). Whether or not these spatial variations correspond to true density structure [i.e. to local fluctuations of $n(H_2)$] is obviously of key importance for the modelling of physical and chemical processes within molecular gas.

To investigate this question, a time variation study of H_2, CH, and CH^+ interstellar absorption lines towards the O9.5V runaway star AE Aur, HD 34078 has been undertaken by Rollinde et al. (2003, hereafter R03) and Boissé et al. (2005, hereafter B05). This bright star is significantly reddened [$E(B-V)$ = 0.53] and its optical spectrum displays strong absorption lines

* Based on observations made mainly at IRAM, Observatoire de Haute Provence (France), McDonald Observatory (USA) and with FUSE.

Article published by EDP Sciences

Table 1. Observation parameters. The projection center of all the data is: $\alpha_{2000} = 05^h16^m18.15^s$, $\delta_{2000} = 34$ deg $18'44.3''$.

Molecule	Transition	Frequency GHz	Instrument	# Pix.	$F_{\rm eff}$	$B_{\rm eff}$	Resol. arcsec	Resol. km s^{-1}	Int. Time hours	$T_{\rm sys}$ K	Noise mK	Obs. date
^{12}CO	$J = 1$–0	115.271202	30 m/AB100	2	0.95	0.74	22	0.20	0.7	240	20	13 Feb. 2004
^{12}CO	$J = 2$–1	230.538000	30 m/HERA	9	0.91	0.52	11	0.40	0.7	300	10	11–13 Feb. 2004

from e.g. CH, CH$^+$, CN (Federman et al. 1994), typical of diffuse molecular clouds. HD 34078 has a high proper motion of $\mu = 43$ mas yr^{-1}, corresponding to a transverse velocity of 103 km s^{-1} or 22 AU yr^{-1} for a distance $D = 530$ pc (this value will be used in the following for consistency with B05; it is compatible with the trigonometric parallax estimate of 446^{+220}_{-111} pc). The line of sight is thus drifting rapidly through the foreground gas; successive column density measurements then provide a "cut" through the cloud revealing its spatial density structure over scales which typically range from 1 to 100 AU for time separations ranging from a few weeks to a few years.

The first five FUSE spectra discussed in B05 showed that highly excited H_2 gas is present along the line of sight, together with more standard quiescent gas at $T \simeq 80$ K. The presence of significant amounts of H_2 with an excitation energy higher that 2500 K (corresponding to the $v = 0, J = 5$ state) is very rare (another remarkable case is that of HD 37903 studied by Meyer et al. 2001). This is certainly related to the fact that by chance, along its long path from the Orion nebula where it was ejected a few millions years ago (Hoogerwerf et al. 2001), HD 34078 has recently encountered a dense interstellar cloud with which it is currently interacting, leading to the present-day appearance of the IC 405 nebula (Herbig 1958).

In previous modelling work of the properties of the gas along the line of sight (B05), it was found that two components are required to account for the observed absorption lines:

- highly excited H_2 located in a bow shock, where the stellar wind impacts on the ambient medium. Illumination of this gas by the strong UV field of the star satisfactorily explains the observed H_2 excitation diagram. The presence of such a bow shock around HD 34078 was suspected on the basis of IRAS data (van Buren et al. 1995) and has been confirmed recently by higher spatial resolution *Spitzer* observations (France et al. 2007);
- a foreground quiescent cloud (supposedly unrelated to HD 34078/IC 405) giving rise to absorption from cold H_2 and other species typical of translucent material (CH, CO, CN).

However, in this scenario, the close similarity of the radial velocity of both components appears as a coincidence. Further, the CH/H_2 ratio towards HD 34078 displays an anomalously high value, about three to four times larger than the one commonly found for other lines of sight. This led us to suspect that HD 34078 might be more closely related to the cold cloud than assumed in the above model, even if at first sight, this appears difficult to reconcile with the low H_2 temperature ($T = 77$ K) derived from the population of the $J = 0$ and $J = 1$ levels and the presence of a variety of molecules that HD 34078 might easily photodissociate.

The potential relation between HD 34078 and the cloud probed has important implications regarding the investigation of small-scale structure. Indeed, in the case of a real association, any mechanical or radiative interaction might significantly affect the initial structure. Further, the gas flow in the bow shock may be subject to instabilities which could lead to time variations of a different nature, not necessarily associated with spatial structure.

Thus, one objective of the present study is to clarify the relation between HD 34078 and the cold cloud. To this end, we have undertaken observations of CO emission in the field surrounding the O star. The second goal of our work is to extend the search for absorption line variations in ground-based spectra (CH and CH$^+$ mainly) and in FUSE spectra (H_2) by adding recent data obtained after the initial studies by R03 and B05 were completed.

This paper is organised as follows. We first present high spatial resolution ^{12}CO(2–1) and ^{12}CO(1–0) observations performed at the 30 m IRAM telescope and their implications concerning the location and properties of the quiescent component (Sect. 2). In Sect. 3, we analyse a new series of optical spectra which allow us to study in detail the variations of CH and CH$^+$ column densities [hereafter N(CH) and N(CH$^+$)] and velocity profiles. Time variations of H_2 column densities [hereafter $N(H_2)$] are then discussed in the light of the observed CH and CH$^+$ variations (Sect. 4). In Sect. 5, we summarize the main observational results for ζ Per and HD 34078, in particular for readers not interested in details concerning observations. Then, we discuss the implications of our observations in terms of processes related to the interaction between HD 34078 and the surrounding gas and small-scale structure in foreground unperturbed gas (Sect. 6). Finally, we summarize our conclusions and present some prospects concerning possible observational signatures of the future evolution of HD 34078's close environment.

2. CO emission towards HD 34078

^{12}CO emission can be used to investigate a possible connection between HD 34078 and the molecules seen in absorption. Indeed, in the two-component model presented in B05, CO molecules (as well as CH, CH$^+$ etc.) lie far in front of HD 34078 and if this picture were correct, the morphology of the CO emission should not correlate in any manner with the star position. Otherwise, any relation between the CO emission map and HD 34078's position would be a clear indication that the star is closely related to the foreground cloud.

2.1. IRAM-30 m observations

Emission of the rotational transitions of ^{12}CO was observed with the IRAM-30 m telescope during three consecutive nights on February 11, 12 and 13, 2004. Using the HERA 3×3 multi-beam array (Schuster et al. 2004), we mapped the ^{12}CO(2–1) emission in a 66×66 arcsec^2 region centred on HD 34078's position. The single side-band receiver temperature was in the range 120 to 180 K. Observations were performed under good weather conditions with 2 mm water vapor and a zenith sky opacity at 230 GHz $\tau_{230} = 0.15$, resulting in system temperatures in the range 250–350 K. Chopper-wheel calibration was done every 10–15 min. Pointing was checked frequently, ensuring an accuracy of $2''$. We used the VESPA autocorrelator as a spectrometer covering 160 km s^{-1} with a resolution power of 7×10^5 or $\delta v = 0.4$ km s^{-1} ($\delta\nu = 0.3$ MHz; see Table 1 for CO

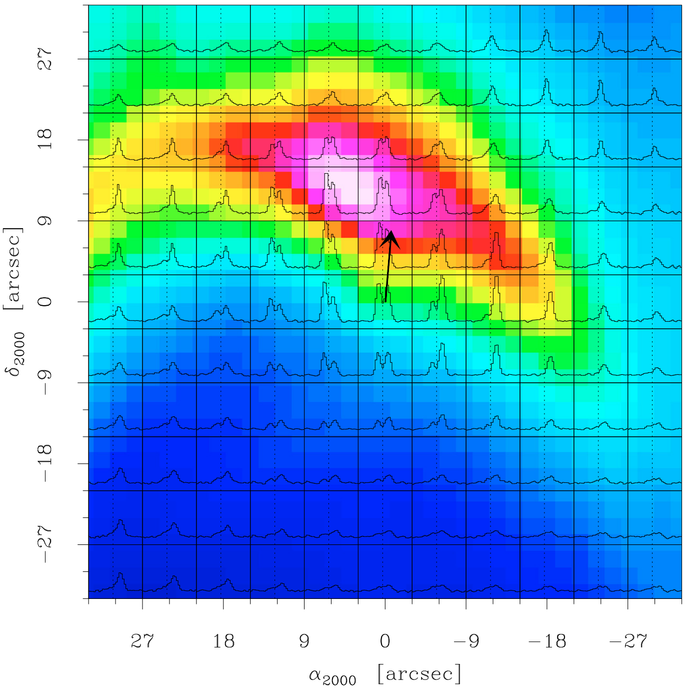

Fig. 1. ^{12}CO(2–1) spectra overlaid on the MIPS 24 μm emission of France et al. (2007) (color scale; note that the IR map is saturated near the maximum at the (3, 12) position). The CO LSR velocity scale is in the range 0–13 km s^{-1} and the antenna temperature scale ranges from −0.1 to 0.6 K. The observed positions correspond to the center of each panel; the dotted line indicates a constant velocity $V_{\rm LSR}$ = 5.9 km s^{-1}, associated with the CH and CH$^+$ lines (see below). HD 34078 is located at offsets (0, 0); the direction of its proper motion is indicated by the arrow.

observation parameter values). Observations were performed in raster mode to allow deep integration of about 40 min to ensure a rms of 15 mK (antenna temperature scale) in each velocity channel. The map consists of a regular grid of 12 × 12 positions observed with a sampling of 6″, and the data are thus only slightly undersampled ($HPBW$ = 11.7″ at 230 GHz). A 5-point cross centred at offsets (−3, 3) with 12″ steps was observed simultaneously with the single-pixel receivers facility, in the ^{12}CO(1–0) and (2–1) transitions ($HPBW$ = 22″ at 115 GHz) to derive the excitation conditions of the gas.

2.2. Results and analysis of the CO data

The resulting map of the ^{12}CO(2–1) emission is shown in Fig. 1, in which the nearly fully-sampled spectra were projected on a 6″× 6″ grid centred on the (0, 0) offset. Thermal dust emission has also been observed recently by France et al. (2007) and their MIPS 24 μm is overlaid by the CO spectra.

We also present a map of the integrated ^{12}CO(2–1) intensity superimposed onto the MIPS 24 μm emission (Fig. 2) as well as channel maps (Fig. 3). The ^{12}CO(2–1) integrated intensity is clearly stronger around the star position (0, 0). While the NE and SW region are nearly devoid of emission, the region of enhanced ^{12}CO(2–1) emission is resolved and displays an elongated morphology (in the NE-SW direction) and extent which are both relatively similar to those of the brightest part of the IR arc. The ^{12}CO(2–1) peak is apparently offset southward by about 9″ with respect to the 24 μm maximum but, given i) the accuracy of absolute positions in the IR map (≃1″; K. France, private communication) and ^{12}CO(2–1) emission (≃2″) and ii) the presence of saturation in the 24 μm map, it is not clear whether this offset is really significant.

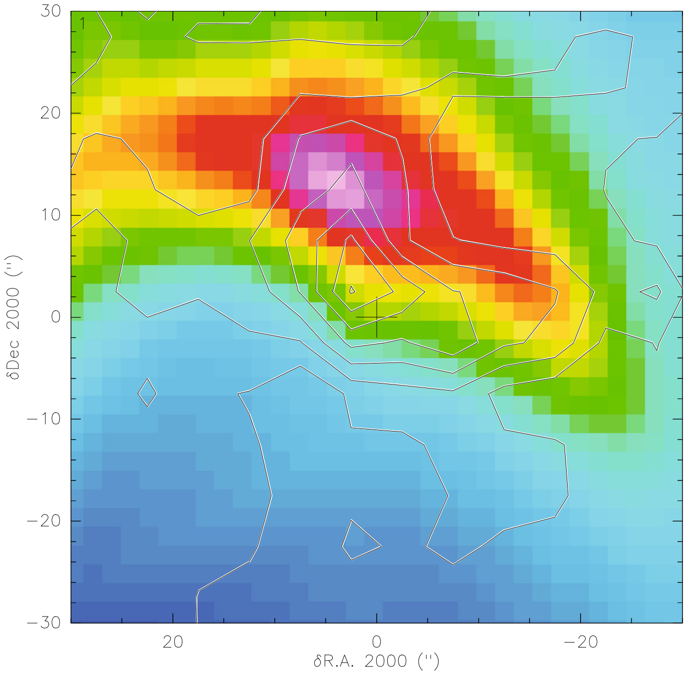

Fig. 2. The integrated ^{12}CO(2–1) emission (contours) overlaid on the MIPS 24 μm emission of France et al. (2007) (color scale). The CO profiles have been integrated in the interval 2.5–10 km s^{-1}; the first contour level and spacing between successive contours is 0.189 K km s^{-1}.

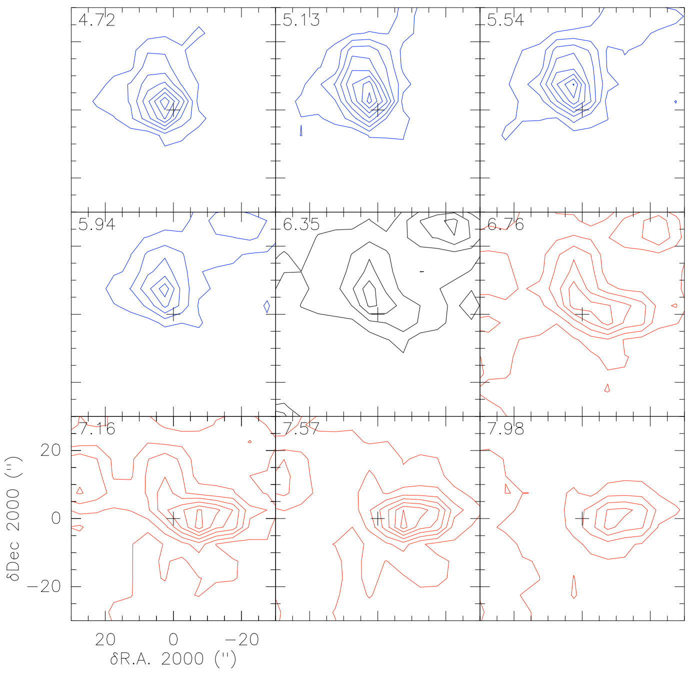

Fig. 3. Channel maps of the ^{12}CO(2–1) emission averaged over an interval of 0.41 km s^{-1}(the value in the upper left corner is the center of the velocity interval considered). Each panel corresponds to the region shown in Fig. 1. The first contour level and spacing between successive contours is 3.5 mK.

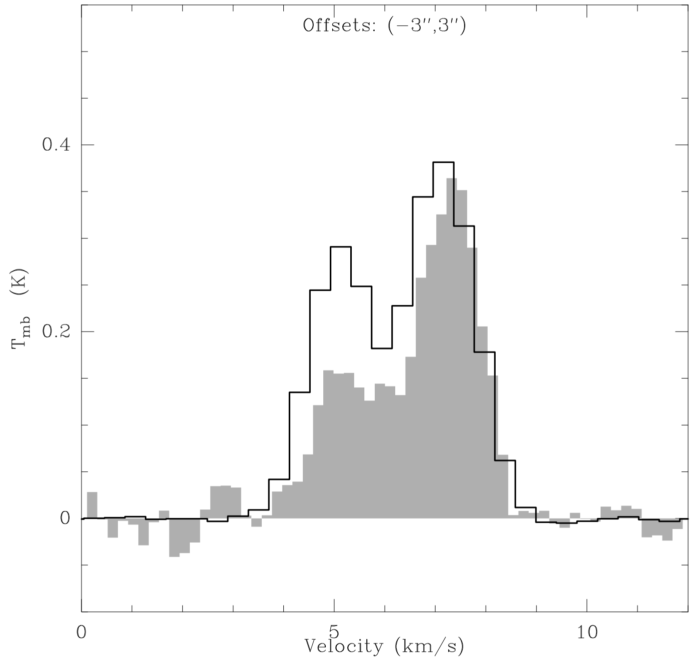

Fig. 4. Emission spectra of ^{12}CO(1–0) (grey scale histogram) and ^{12}CO(2–1) (thick line) centred at the (–3, 3) offset. ^{12}CO(2–1) spectra from adjacent positions were convolved to synthetize the ^{12}CO(2–1) emission in the 22″ (1–0) Gaussian beam (see text). Main beam temperatures are adopted.

The profiles are double peaked close to the star (in an approximate circle of diameter 20–30″; note the blue and red components appearing on each side of the vertical dotted line at 5.9 km s^{-1} plotted in Fig. 1). The spectra closest to the star display a mirror symmetry about an axis coincident with HD 34078's path, with the blue emission line stronger to the E and the red one stronger to the W. This is apparent in the channel maps (Fig. 3), where the red component peaks to the W while the blue one peaks to the NE. The symmetry quickly disappears as the profiles become single peaked further away. Averaging spectra in the NW or SE areas clearly shows that weak wings are present there over the entire velocity range (V_{LSR} = 3–10 km s^{-1}) covered by the more intense emission seen in the central part. The systemic velocity of the ambient molecular gas is $V_{LSR} \simeq$ 6.5 km s^{-1}.

We now consider the additional ^{12}CO(1–0) spectra (Fig. 4) to investigate the excitation of the CO gas at the (–3, 3) position (at other positions, the ^{12}CO(1–0) spectra are of lower S/N due to a shorter integration time and are less appropriate to measure the excitation ratio). For this purpose, ^{12}CO(1–0) and ^{12}CO(2–1) spectra are brought into the main beam temperature scale; the forward and beam efficiencies are given in Table 1. We next synthetize the ^{12}CO(2–1) emission over the (1–0) beam using the spectra obtained at adjacent positions [(–9, 3), (–3, 9), (3, 3), (–3, –3)] with the appropriate weighting. The resulting (2–1)/(1–0) integrated intensity ratio appears to be around 1.5, a large value compared to that (≃0.7) commonly observed towards diffuse clouds (Falgarone et al. 1998; Liszt & Lucas 1998; Pety et al. 2008). Moreover, the (2–1)/(1–0) ratio is significantly different for the two main components around V_{LSR} ≃ 5 and 7 km s^{-1} for which we obtain values of about 1.8 and 1.3, respectively.

The above results on the (–3, 3) position can be used to set constraints on the physical conditions prevailing in the gas. With the help of a large velocity gradient model (Hily-Blant & Falgarone 2007), we find that acceptable solutions can be obtained for T > 12 K and that above T = 20 K, the gas density is well constrained and must lie in the range $n = 10^3$–10^4 cm^{-3} (n is the ambient H number density). All solutions obtained correspond to optically thin emission. For instance, at T = 80 K, a value close to the temperature estimated for the dust by France et al. (2007), we get $n = 2 \times 10^3$ cm^{-3} and N(CO) = 3.7×10^{14} cm^{-2} at V_{LSR} = 5 km s^{-1} and $n = 1.8 \times 10^3$ cm^{-3} and N(CO) = 6.0×10^{14} cm^{-2} for the V_{LSR} = 7 km s^{-1} component. Note that the above CO column densities are comparable to the value N(CO) = 5.7×10^{14} cm^{-2} inferred either from IUE data by McLachlan & Nandy (1984) or from FUSE by Sheffer et al. (2008) for the gas *in front of* HD 34078.

We end this section by concluding that our CO observations allow us to unambiguously answer the question which motivated this study: HD 34078 is indeed closely associated with molecular gas located in its immediate vicinity (which was previously assigned to a foreground quiescent cloud by B05). Moreover, the anomalous CO excitation observed, the large inferred gas density and peculiar velocity field very likely result from the interaction between the stellar wind/radiation and the ambient molecular material (in Sect. 6, we discuss in more detail the implications of the CO observations).

3. Variation of CH and CH$^+$ absorption lines

3.1. Description of optical observations

In the visible, we add 26 spectra to the data considered in R03. Twelve spectra were taken at OHP, eight at McDonald Observatory (hereafter McD) while three spectra were obtained at the Boyunsan Optical Astronomy Observatory (BOAO, South Korea), two at the Terskol Observatory and one at Calar Alto. Altogether, these observations probe the evolution of CH and CH$^+$ abundances between 1989 and 2008, with good sampling since 2000. In particular, our recent data well cover the period during which the eight FUSE spectra were obtained. The date of each observation and spectral resolution are given in Table 2.

To check in a direct way the consistency of measurements performed at different telescopes, in 2003 we started parallel observations of the bright star ζ Per. The latter has been observed in nearly all OHP and McD runs, in addition to HD 34078 (cf. Table 2). This nearby reddened star [d = 400 pc, $E(B-V)$ = 0.33] has a small proper motion of 10.2 mas yr^{-1}, corresponding to a transverse velocity of 4.1 AU yr^{-1}, much smaller than the value for HD 34078 (22 AU yr^{-1}). Thus, in principle we expect much less variation due to structure in the foreground IS gas towards ζ Per and absorption lines seen in the spectra of that star should be a good indication of the instrumental stability and homogeneity of our measurements. Data from the literature (Allen 1994; Crane et al. 1995) do show that W_λ values for CH, CH$^+$, CN, Ca I, and Ca II are constant within errors for ζ Per.

OHP observations were made in service mode using the ELODIE spectrograph (Baranne et al. 1996), as in R03, except for the four latest runs which were performed with SOPHIE, the new spectrograph that now supersedes ELODIE at the 1.93 m telescope (Bouchy & The Sophie Team 2006). SOPHIE provides an improved spectral resolution (R = 75 000) and sensitivity, as well as an extended wavelength range (including CH λ3886, CH λ3890, and CH$^+$ λ3957; as the blue CN lines are close to the blue edge of the spectra the S/N is too low for these features to be usable). Since SOPHIE has been optimized for the detection of extrasolar planets by radial velocity measurements, it

Table 2. List of observations and measured CH and CH$^+$ equivalent widths (in mÅ; uncertainties as estimated in Sect. 3.2.1 are given in upper index).

Epoch	Observatory	R^a	W_{4300}(CH) [mÅ] HD 34078	W_{4232}(CH$^+$) HD 34078	W_{4300}(CH) ζ Per	N(CH)^c HD 34078	N(CH$^+$)^c HD 34078
2002.73	OHP/ELODIE^b	32 000	$57.35^{0.92}$	$47.30^{1.51}$	—	$0.97^{0.02}$	$0.69^{0.02}$
2003.15			$54.06^{0.76}$	$44.50^{1.19}$	$15.05^{0.39}$	$0.89^{0.01}$	$0.63^{0.02}$
2003.71			$52.36^{0.93}$	$46.44^{1.30}$	$16.22^{0.46}$	$0.85^{0.02}$	$0.67^{0.02}$
2003.96			$55.54^{1.77}$	—	$15.26^{0.58}$	$0.92^{0.03}$	—
2004.15			$51.94^{0.81}$	$46.66^{1.30}$	$16.22^{0.99}$	$0.84^{0.01}$	$0.67^{0.02}$
2004.88			$54.70^{1.20}$	—	—	$0.90^{0.02}$	—
2005.72			$51.30^{0.90}$	$45.36^{1.40}$	$15.16^{0.64}$	$0.82^{0.01}$	$0.65^{0.02}$
2006.11			$48.97^{0.95}$	$42.01^{1.40}$	—	$0.77^{0.01}$	$0.58^{0.02}$
2006.71	OHP/SOPHIE	75 000	$54.91^{0.32}$	$44.23^{0.52}$	$15.98^{0.13}$	$0.909^{0.005}$	$0.623^{0.007}$
2007.14			$51.00^{0.51}$	$41.30^{0.45}$	$16.01^{0.26}$	$0.815^{0.008}$	$0.563^{0.006}$
2007.67			$53.30^{0.36}$	$45.33^{0.47}$	$16.05^{0.13}$	$0.869^{0.006}$	$0.646^{0.007}$
2008.10			$54.16^{0.30}$	$48.29^{0.43}$	$16.22^{0.15}$	$0.890^{0.005}$	$0.710^{0.006}$
2003.00	McDonald	170 000	$55.50^{0.28}$	$44.78^{0.45}$	$15.80^{0.14}$	$0.880^{0.004}$	$0.632^{0.006}$
2004.02			$52.10^{0.32}$	$47.00^{0.51}$	$14.90^{0.36}$	$0.816^{0.005}$	$0.672^{0.007}$
2004.76			$50.80^{0.69}$	—	$15.70^{0.29}$	$0.816^{0.01}$	—
2004.98			$53.10^{0.33}$	$47.30^{0.57}$	$15.70^{0.18}$	$0.843^{0.005}$	$0.697^{0.008}$
2005.81			$49.00^{0.26}$	$44.90^{0.60}$	$16.00^{0.08}$	$0.763^{0.004}$	$0.636^{0.009}$
2005.99			$49.90^{0.22}$	$43.50^{0.60}$	$16.15^{0.11}$	$0.774^{0.003}$	$0.613^{0.008}$
2007.02			$53.20^{0.40}$	$42.70^{0.42}$	$15.88^{0.18}$	$0.832^{0.006}$	$0.595^{0.006}$
2008.00			$54.34^{1.08}$	$47.88^{1.64}$	$15.74^{0.15}$	$0.90^{0.02}$	$0.68^{0.02}$
2004.10	BOAO	30 000	$52.50^{0.45}$	—	—	$0.850^{0.007}$	—
2004.18	BOAO-Terskol	30 000–120 000	$50.67^{0.35}$	—	—	$0.807^{0.006}$	—
2006.77	BOAO	45 000	$54.60^{0.62}$	$44.40^{0.60}$	—	$0.90^{0.01}$	$0.627^{0.008}$
2004.65	Terskol	120 000	$55.00^{0.45}$	—	—	$0.911^{0.007}$	—
2007.18	Calar Alto	40 000	$52.15^{0.88}$	$41.80^{0.95}$	—	$0.84^{0.02}$	$0.57^{0.01}$

[a] Resolution near CH λ4300. [b] W_{4300}(CH) and W_{4232}(CH$^+$) values from OHP/ELODIE spectra have been corrected by +6% and +8% respectively (see text). [c] Column densities in units of 10^{14} cm^{-2}, measured directly from line profiles for high resolution spectra (McDonald) or computed from W values using Eqs. (1) and (2) for other data.

provides an accurate wavelength scale (better than 0.01 km s^{-1}; this scale is relative to the barycentre of the solar system). Each observation consisted of 4 to 8 individual exposures totalling about 1 h for HD 34078 and 10$^{\rm m}$ for ζ Per; these two targets were generally observed consecutively or, occasionally, during two successive nights. Spectra were extracted using the pipeline data reduction software. The latter were designed specifically for these spectrographs (Baranne et al. 1996; Bouchy & The Sophie Team 2006) and include all required steps (in particular bias and flat field corrections, using appropriate exposures). For observations of bright stars such as ζ Per and HD 34078, this procedure has been shown to work efficiently, which we checked whenever it was possible, e.g. by comparing independent spectra taken at short time intervals before merging them, or by comparing W values for those lines seen twice, on two consecutive orders.

At McDonald Observatory echelle spectra of HD 34078 were obtained with the Harlan J. Smith 2.7 m telescope. The strongest molecular features from CN, CH$^+$, and CH are detected, as are the K line of Ca II and Ca I λ4226, although the latter falls next to a CCD glitch and thus cannot be reliably extracted. The data were reduced in the same fashion as before (cf. R03). A global multi-order fit of the entire CCD chip was performed for each Th-Ar spectrum, yielding residuals below 0.001 Å (or 0.08 km s^{-1}). Measured radial velocities of (non-variable) absorption lines towards the comparison star ζ Per show a scatter that is consistent with the residuals from the wavelength calibration. From the Th-Ar data we measured the instrumental resolution of our spectra, which turned out to be R = 170 000. Stellar exposures were 30$^{\rm m}$ long for HD 34078, and typically 5$^{\rm m}$ for ζ Per.

A few observations of HD 34078 were also performed at other telescopes. Two spectra were obtained using the MAESTRO spectrograph, fed by the 2-m telescope at the Terskol Observatory (TE) in Northern Caucasus (the resolution was 120 000). Three more spectra were obtained using the fiber-fed echelle spectrograph installed at the 1.8-m telescope of the Bohyunsan Optical Astronomy Observatory (BOAO) in South Korea (a description can be found in Galazutdinov et al. 2005). Modes providing resolutions, R = 30 000 or 45 000, were employed (Table 2). Finally, a spectrum was taken in service mode at the Calar Alto observatory with the FOCES spectrograph (R = 40 000, Pfeiffer et al. 1998). For these additional runs, ζ Per was not observed; we are nevertheless confident that these data are homogeneous with respect to the other spectra obtained.

3.2. Equivalent widths and column densities

3.2.1. Equivalent width estimates

Equivalent width measurements were performed in a similar way as in R03 for CH λ4300. Regarding W_{4232}(CH$^+$), the accuracy is limited by the poor definition of the continuum due to blending with a stellar line (cf. Fig. 7 in R03). Then, to avoid possible resolution-dependent effects on the estimate of W values and to improve the homogeneity and accuracy of our measurements, we fitted this stellar line with a Gaussian. Its

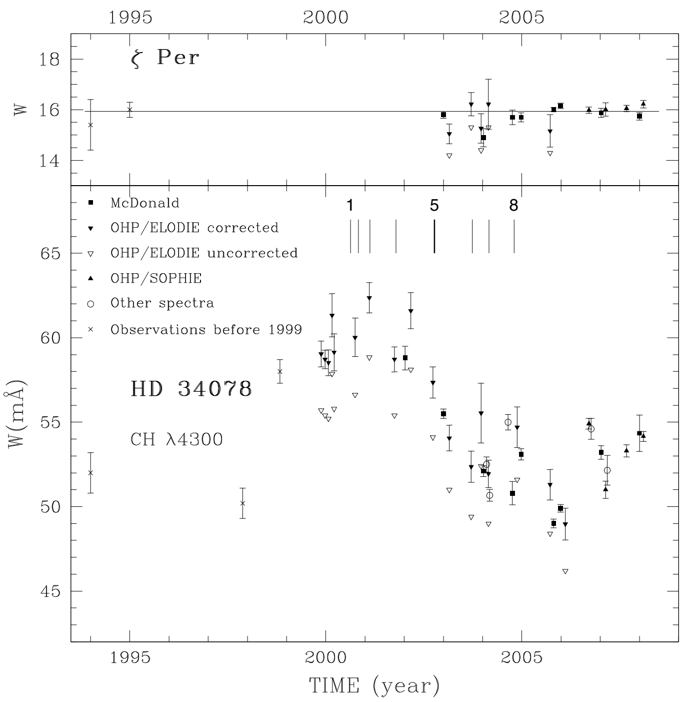

Fig. 5. Equivalent widths of CH λ4300 measured in HD 34078 (*lower panel*) and ζ Per (*upper panel*) spectra (see Table 2). Open triangles correspond to raw OHP/ELODIE values, which appear systematically too low (filled triangles correspond to corrected values, see text). Tick marks numbered 1 to 8 show the epochs at which the FUSE spectra were taken.

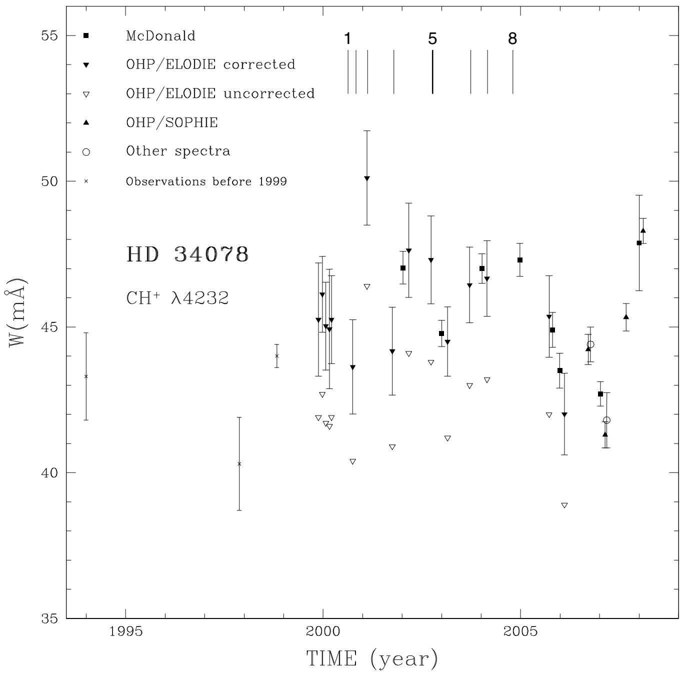

Fig. 6. Same as in Fig. 5 but for the equivalent widths of CH$^+$ λ4232 in HD 34078 spectra. Raw OHP/ELODIE values (empty triangles) have been corrected by +8% (filled triangles).

position ($\delta\lambda = -0.364$ Å with respect to the CH$^+$ absorption) and *FWHM* (0.46 Å) were fixed while the depth was varied so as to match the continuum blueward of the CH$^+$ absorption as well as possible (a typical value for the depth is 3% of the continuum). Once the spectra have been normalised in this way, we measure W and its uncertainty as done for CH λ4300. This procedure was applied to all spectra, including those obtained prior to 2003; for the latter, this results in W values which differ slightly from those given in R03.

Some observations of HD 34078 were spread over 2 or 3 consecutive nights (in particular the recent, high S/N, McD and OHP/SOPHIE spectra), which allowed us to check that no significant day-to-day variations are present; we then measured W on the co-added spectrum. For the same reason, one BOAO and one TE measurement obtained two days apart in March 2004 were combined (thus Table 2 contains 25 entries).

Uncertainties were estimated in a conservative way, including the error due to finite pixel-to-pixel S/N ratio and the one in continuum placement; we assume as in R03 that the two sources of errors combine quadratically. W estimates for HD 34078 and their associated errors are given in Table 2 for HD 34078 (CH λ4300 and CH$^+$ λ4232) and ζ Per (CH λ4300); note that concerning OHP/ELODIE spectra, values corrected as explained below are given for both HD 34078 and ζ Per.

3.2.2. Consistency of all measurements

In Fig. 5 (upper panel), we show results from the CH λ4300 ζ Per observations performed between 2003 and 2007, to which we add older measurements from Crane et al. (1995) and Allen (1994). These are consistent with a constant value of W_{4300}(CH). However, careful examination reveals a small offset of about –6% for the OHP/ELODIE values with respect to the other measurements. Since the same offset appears to be present in the HD 34078 W_{4300}(CH) values (lower panel, empty triangles), this effect is very likely due to scattered light in the ELODIE spectrograph (Ilovaisky and Prugnel, personal communication). Thus, we applied a +6% correction (scattered light from the target does lead to a multiplicative correction on W values) to all OHP ELODIE CH λ4300 values (filled triangles), including those presented in R03.

Unfortunately, the CH$^+$ λ4232 line towards ζ Per is too faint ($W \simeq 2.5$ mÅ) to assess whether OHP/ELODIE measurements of this transition are also affected by scattered light. Then, to determine the correction for CH$^+$ λ4232 (which may be different from that for CH λ4300), we have to rely on the HD 34078 data themselves (Fig. 6). By comparing the sets of OHP and McD values, we find that an offset of about +8% needs to be applied to the OHP/ELODIE values to bring both sets of points to good mutual agreement (filled triangles in Fig. 6). After correcting the OHP/ELODIE W values in this way, it is apparent in Figs. 5 and 6 that nearly simultaneous measurements performed at different telescopes yield consistent values, within errors. This is a direct indication that uncertainties are not underestimated and that, after correction of the OHP/ELODIE W values, the whole set of data is homogeneous.

The OHP/ELODIE W measurements of CH$^+$ λ3957 are not accurate enough in comparison to those for CH λ4300 or CH$^+$ λ4232 to be really useful (further, they are affected by scattered light in an unknown way). In contrast, the recent OHP/SOPHIE spectra provide good S/N values for W_{3957}(CH$^+$). In Fig. 7 (panels c and d) we show the variation of W versus time for both CH$^+$ transitions since September 2006; as can be seen, the two sets of measurements are very consistent. We also display for the same epochs the behavior of W_{4300}(CH) for both

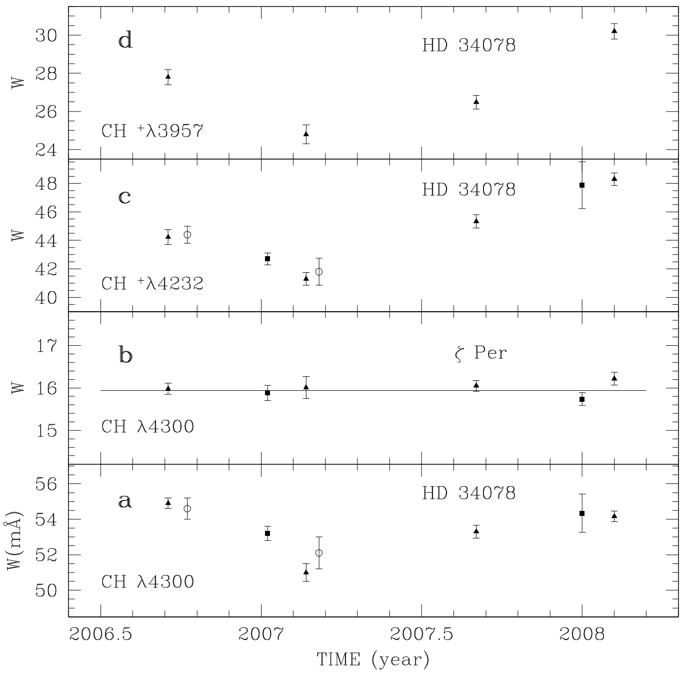

Fig. 7. Equivalent width of CH λ4300 **a)**, CH$^+$ λ4232 **c)** and CH$^+$ λ3957 **d)** in HD 34078 spectra since September 2006 (symbols used have the same meaning as in Fig. 5). The equivalent width of CH λ4300 in ζ Per spectra **b)** is shown for comparison (the horizontal line corresponds to the weighted average of the displayed values). Note the similarity between both CH$^+$ transitions and the good CH–CH$^+$ correlation.

HD 34078 (panel a) and ζ Per (b); the latter values remained constant while the variations seen for CH in HD 34078 are qualitatively similar to those observed for CH$^+$. The whole set of values for W_{4232}(CH$^+$) and W_{4300}(CH) shows a fairly smooth variation, with apparently little or no variations with timescales smaller than a few months.

Figures 5–7 strongly suggest that the equivalent widths varied for HD 34078 while W_{4300}(CH) remained constant for ζ Per. Let us now assess in a quantitative way the statistical significance of time changes in the observed W values. To this end, we perform a χ^2 test on W_{4300}(CH) values for both the ζ Per and HD 34078 sets of measurements, in order to check whether the assumption of a constant W can be accepted or rejected. Using the whole data set, we find that the ζ Per data are consistent with a constant value, W_{4300}(CH) = 15.93 mÅ, while the assumption of a constant W value can be rejected at the 5.2σ level for HD 34078 (the W value which minimizes χ^2 is 52.3 mÅ). Note that these conclusions are unchanged if the OHP/ELODIE data are removed. Equivalently, if the distribution of $x = (W - \langle W \rangle)/\sigma$ values is compared to a Gaussian with $\sigma_x = 1$, one finds that it is consistent for ζ Per values and inconsistent for HD 34078 (the χ^2 test described above is just a way to quantify these statements). We can therefore conclude that real time variations of W_{4300}(CH) occurred during the 2003–2008 period for HD 34078 (for CH$^+$ towards HD 34078, the assumption of a constant W is rejected at the 3.2σ level).

3.2.3. From equivalent widths to column densities

Since the absorption lines considered here are not completely optically thin, we cannot infer N values directly from W ones. We will then rely on the highest resolution data, from McD observations. In the latter, the CH$^+$ λ4232 profiles are fully resolved; one can thus derive the true optical depth and get N(CH$^+$) by direct integration. Regarding CH, the determination of N and of the velocity profile is complicated by the structure of the ground level, due to Λ doubling. As shown by Lien (1984), neglecting this effect may cause an underestimate in N(CH) and a broadening of the profile, when the intrinsic width is small enough (i.e. comparable to or smaller than the splitting of the ground level, which corresponds to 1.43 km s^{-1}).

CH profiles include at least two components (a strong asymmetric and narrow one superimposed on weak shallow absorption) and fitting with Voigt profiles remains somewhat arbitrary (Figs. 5 and 7 in R03). Thus, to get the intrinsic CH pixel optical depth profile without any a priori decomposition and perform the detailed comparison with the CH$^+$ profile allowed by the quality of the McD data, we use a Bayesian inversion procedure as done by Pichon et al. (2001) in the context of Lyα absorption in QSO spectra. Equally populated sublevels are assumed (we checked that the relative strength of the CH λ3886 and CH λ3890 lines in the OHP/SOPHIE spectra is consistent with this hypothesis; see also Lien 1984, for other lines of sight). We find in the end that taking into account Λ doubling induces corrections on N(CH) which are no larger than 1.3%.

Significant changes in the CH and CH$^+$ profiles are seen (see Sect. 3.3) but these remain relatively small and further, the optical thickness of either CH λ4300 or CH$^+$ λ4232 does not exceed 1. One can therefore expect a simple empirical relation to hold between W and N, allowing us to infer N values from W measurements performed from lower resolution data. In Fig. 8, we show W/λ versus $Nf\lambda$ for both CH λ4300 and CH$^+$ λ4232 from McD spectra. As can be seen, both sets of points are well fitted by a single straight line (dotted line), as a result of the similarity of CH and CH$^+$ velocity profiles (cf. R03 and Sect. 3.3). This fit corresponds to the following relations,

$$N(\mathrm{CH}) \;=\; 2.42 \times 10^{11} W^{1.48} \tag{1}$$

and

$$N(\mathrm{CH}^+) \;=\; 2.29 \times 10^{11} W^{1.48} \tag{2}$$

for CH λ4300 and CH$^+$ λ4232 respectively, with W in mÅ and N in cm^{-2}. It is noteworthy that although we made no assumption on the shape of line profiles in the above procedure, the best fit turns out to be close to the curve of growth for a single Gaussian component with b = 3.2 km s^{-1}. All measurements are nicely bracketted by curves of growth with b values between 2.8 and 3.5 km s^{-1}. We next assume that the $N(W)$ best fit relation holds at all epochs and use it to infer N from W for measurements other than the McD ones. In Table 2, we list N(CH) and N(CH$^+$) values; for McD spectra, these are drawn directly from line profiles while for lower resolution data, N is obtained from W through Eqs. (1) and (2). The resulting uncertainty in N should in principle involve two terms, one related to the errors on W and the other to the scatter about the best fit; in practice, the latter appears to be small and we ignore it.

3.2.4. CH and CH$^+$ column density variations

Figure 9 shows the variation of N(CH) and N(CH$^+$) observed between 1998 and 2007. In R03 we found that W_{4300}(CH) increased from 1990 to 2002; the +6% applied to the OHP/ELODIE data results in a larger amplitude for this variation (21% instead of 14%). It now appears that N(CH) reached a maximum during the 2000–2002 interval, and has been decreasing since then to reach in 2006 a value similar to those

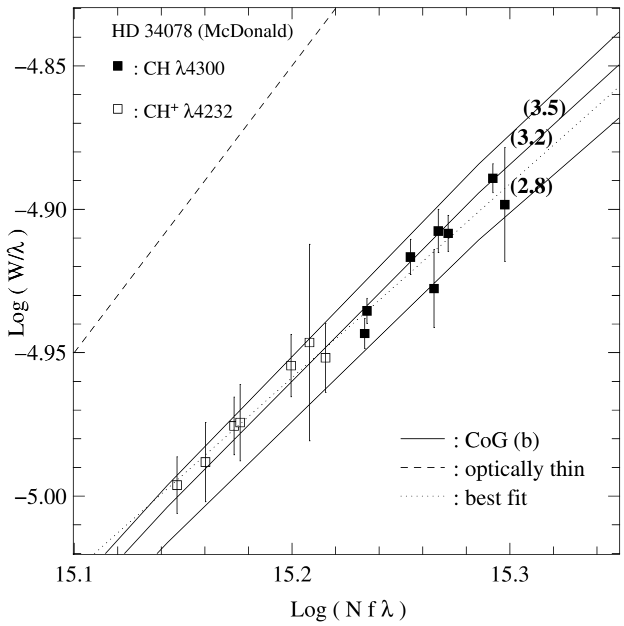

Fig. 8. Equivalent width versus column density for high resolution observations (McDonald). CH (filled squares) and CH^+ (empty squares) absorption lines span different ranges in opacity which helps to constrain the best linear fit (dotted line: $y = -15.232 + 0.676\,x$). A curve of growth with $b = 3.2$ km s^{-1} also provides a good fit to the data (plain line; the two additional lines correspond to $b = 2.8$ and $b = 3.5$ km s^{-1} and bracket the data points well). The large b curve (i.e. optically thin limit) is shown (dashed line).

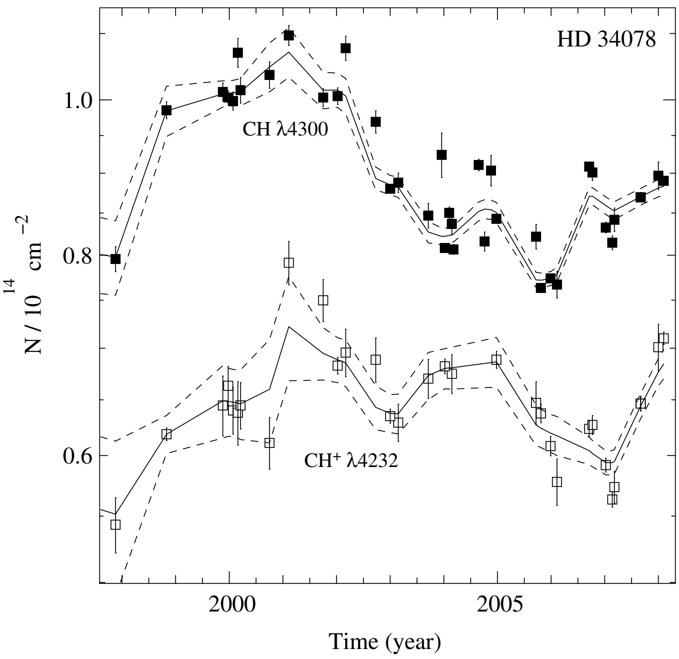

Fig. 9. Evolution of the CH and CH^+ column densities with time. The solid thick lines show the long-term evolution obtained after smoothing using a Gaussian window with a $FWHM$ of one year (dashed lines indicate $\pm 3\sigma$ bounds on smoothed values).

observed before 1998. To better characterise the long-term variation, we smoothed the data using a Gaussian window with a $FWHM$ of one year. In the averaging, each N value is weighted according to $1/\sigma^2(N)$ where $\sigma(N)$ is the uncertainty; the resulting curve (together with $\pm 3\sigma$ bounds) is shown in Fig. 9. The typical timescale for these variations, τ_N, defined as the time needed for N to change by 10% (i.e. $\tau_N = [\mathrm{d}N/(0.1N\mathrm{d}t)]^{-1}$) is about 1.5–2 yr.

The new data clearly indicate that additional variations, with shorter timescales, are also present as was suspected from earlier data (R03). This is especially clear in the most recent 2006–2008 results: N(CH) decreased by −10% between September 2006 and February 2007, ($\tau_N \simeq 0.5$ yr) and then increased by 9% to reach the last February 2008 value (see Fig. 7 for a zoom on the recent W data).

We now consider the CH^+ measurements shown as empty squares in Fig. 9. The +8% correction applied to the OHP/ELODIE data somewhat affects the previous conclusion of R03 of a possible decrease of $N(CH^+)$ between 1990 and 2002: $N(CH^+)$ now looks essentially constant over the long term, with no large amplitude variations such as those seen for CH. Beyond 2000, the general pattern is relatively similar for both species. However, although the long-term variations in CH and CH^+ seem to be loosely correlated, there is a good correspondence between the short-term ones; this is especially clear in Fig. 7 (note in particular the coincidence of the local minima in February 2007 for both species). Although the variation patterns are qualitatively similar, the amplitudes are significantly different. For instance, the increase of $N(CH^+)$ between February 2007 and 2008 (+26%) is notably larger than that of N(CH) (+9%).

We shall now focus on the high resolution spectra of the CH λ4300 and CH^+ λ4232 absorption lines in order to investigate whether the observed long and short-term variations in W are accompanied by detectable changes in line profiles. Profile variations might also be present which are not necessarily reflected in appreciable W changes.

3.3. *High resolution CH and CH+ line profiles and their variations*

The high resolution profiles obtained at McDonald Observatory have all been corrected for the Doppler shift due to the Earth velocity and have been brought in the LSR system. Yet, after correction, the wavelength of the ζ Per CN and CH lines still show slight fluctuations in position (of at most a few mÅ) from one epoch to another (given the excellent S/N and the sharp line profiles, misalignments by only a few mÅ are sufficient to induce significant profile differences). These fluctuations are identical for both CN and CH lines to within 1 mÅ and show a good correlation with those of the HD 34078 lines. They must then be due to some inaccuracy in the LSR correction from one epoch to another. To improve the accuracy in the alignment of the HD 34078 absorption lines, we assume that ζ Per lines have been stable in position (this is confirmed by SOPHIE spectra whose wavelength scale is accurately defined) and infer the value of the relative shifts for each epoch. These are used to slightly adjust the position of HD 34078 lines.

The CH and CH^+ line profiles are quite similar (Fig. 10): both include a narrow component with a full width at half maximum of about 5.5 km s^{-1} (corresponding to a b parameter of 3.3 km s^{-1}) and shallow absorption extending from −4 up to 17 km s^{-1}. The CH and CH^+ narrow components cover the same velocity range ($\simeq$2–11 km s^{-1}) but their shapes are significantly different: CH displays a steeper blue edge, while the opposite holds for CH^+. This results in a shift of about +1.6 km s^{-1} for the CH^+ line centre with respect to that of CH. It is

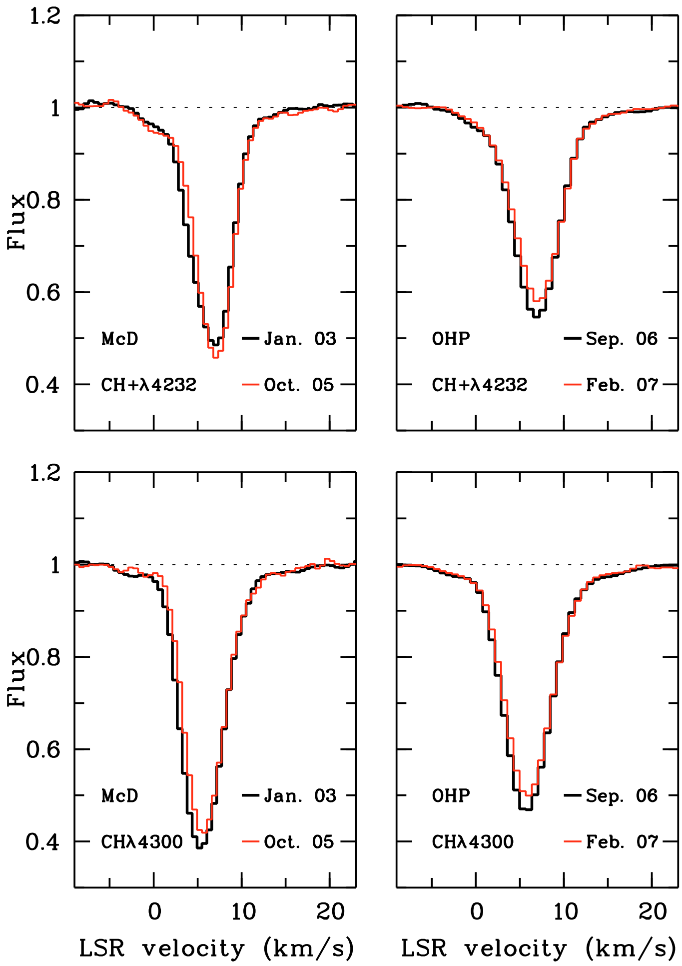

Fig. 10. Comparison of McD CH λ4300 (*lower left*) and CH$^+$ λ4232 (*upper left*) profiles observed in January 2003 and October 2005. During this 2.81 yr time interval W varied by −11.7% and +0.3% respectively. Same for OHP/SOPHIE CH λ4300 (*lower right*) and CH$^+$ λ4232 (*upper right*) profiles obtained in September 2006 and February 2007 (W variation of –7.1% and –6.6 % over 0.43 yr). Note the good stability of the red side of the profiles.

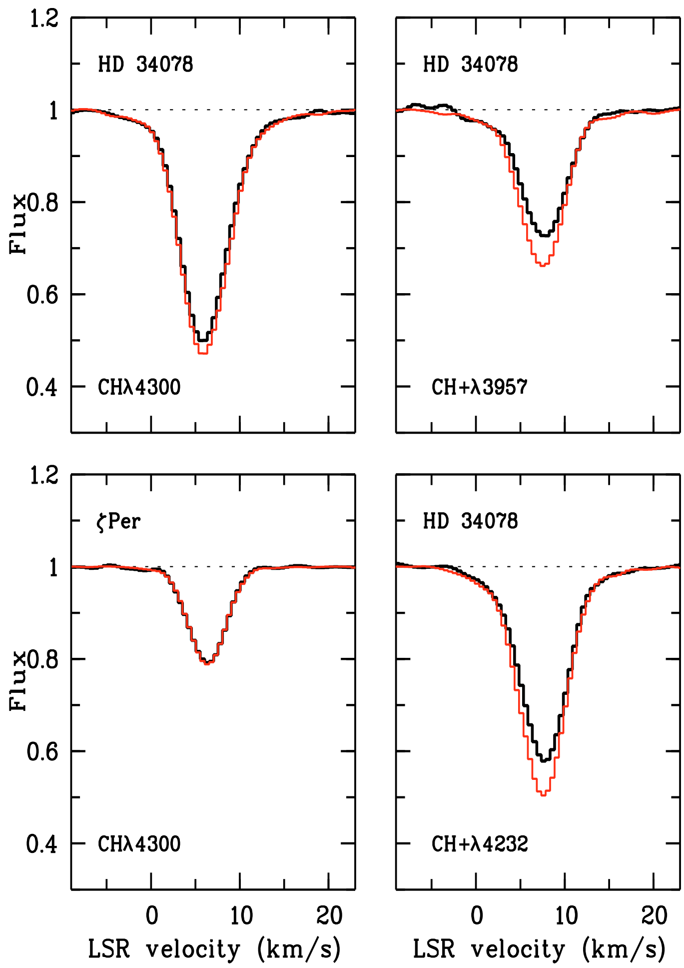

Fig. 11. Comparison of the HD 34078 OHP spectra obtained in February 2007 (thick line) and February 2008 (thin line) for the CH λ4300 (*upper left*), CH$^+$ λ4232 (*lower right*) and CH$^+$ λ3957 (*upper right*) lines. Note the good consistency between the two CH$^+$ transitions. During this 1.0 yr interval, the ζ Per CH λ4300 profile remained stable (*lower left*).

noteworthy that the velocity range covered by the narrow CH or CH$^+$ absorption coincides quite well with the range over which CO emission is observed.

Since we are likely probing molecular gas closely associated with HD 34078 (i.e. with peculiar physical conditions), one may wonder whether the CH and CH$^+$ profiles show significant differences to those seen on other lines of sight. We note that the presence of a weak broad component is rare (Crane et al. 1995; Crawford 1995) but such shallow absorption would be difficult to detect in most spectra; one of very low amplitude ($\simeq$1% instead of $\simeq$5% in our spectra) is however present in the very high S/N spectrum of ζ Oph presented by Crane et al. (1991).

By comparing successive spectra, we find that fluctuations in W are most often associated with changes in the blue and central part of the profiles, the red side suffering very little variation. This is apparent in Fig. 10 (left panels) in which we display CH McD profiles for the January 2003 and October 2005 epochs. During this 2.8 yr time interval W_{4300}(CH) decreased by 12% and the $FWHM$ of the narrow component decreased by 5%. W_{4232}(CH$^+$) remained nearly constant over the same period but significant profiles changes are nevertheless clearly present; the line is slightly deeper, which compensates for a decrease in $FWHM$ comparable to that seen for CH. Another example is shown in Fig. 10 (right panels), where we compare OHP/SOPHIE CH and CH$^+$ profiles taken over a much shorter interval (0.43 yr from September 2006 to February 2007). In this case, W_{4300}(CH) and W_{4232}(CH$^+$) have decreased by a comparable amount ($\simeq$7%) while both profiles became slightly narrower. Thus correlated W variations appear to be associated with similar profile changes. Since 2003, W values show no systematic trend but rather erratic fluctuations; the same is true for profiles and generally, for two epochs with comparable W values, the profiles are quite similar (the CH$^+$ λ4232 January 2003 and October 2005 profiles being an exception). In Fig. 11 we display the recent February 2007 and 2008 CH and CH$^+$ profiles; the latter show a marked increase in W (cf. Fig. 7), corresponding to +26% for N(CH$^+$) (note that during the same interval, the CH λ4300 ζ Per profile remained stable). We do not see appreciable variations of the broad shallow component, but given its weakness, the significance of this result is limited.

Unfortunately, the S/N ratio for the CN line profiles of HD 34078 is not sufficient to allow a search for variations with a sensitivity comparable to the one attained for CH and CH$^+$. Further, the strongest CN line is clearly affected by variations of blended stellar (C IV) absorption. Thus we shall not discuss variations of CN features.

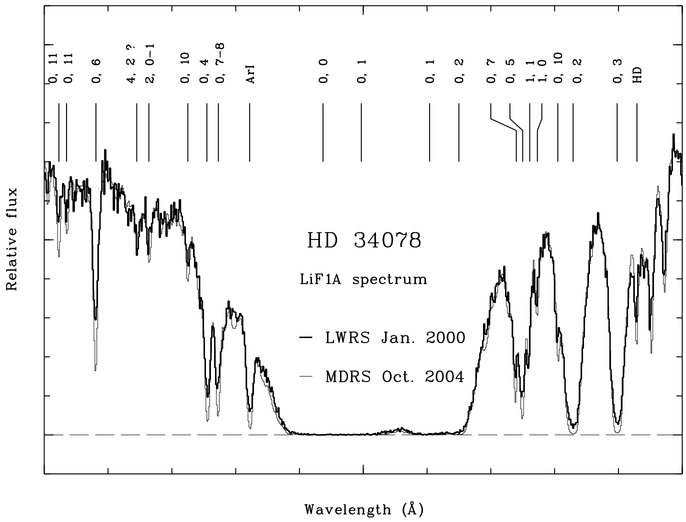

Fig. 12. Comparison of the FUSE spectra obtained in January 2000 (LWRS, thick line) and October 2004 (MDRS, thin line) in the region around 1050 Å (v and J values for the lower level of each H_2 transition are indicated; the HD line is from J = 0). In the MDRS spectrum, narrow lines tend to appear deeper and the damped (0, 0) and (0, 1) features slightly broader.

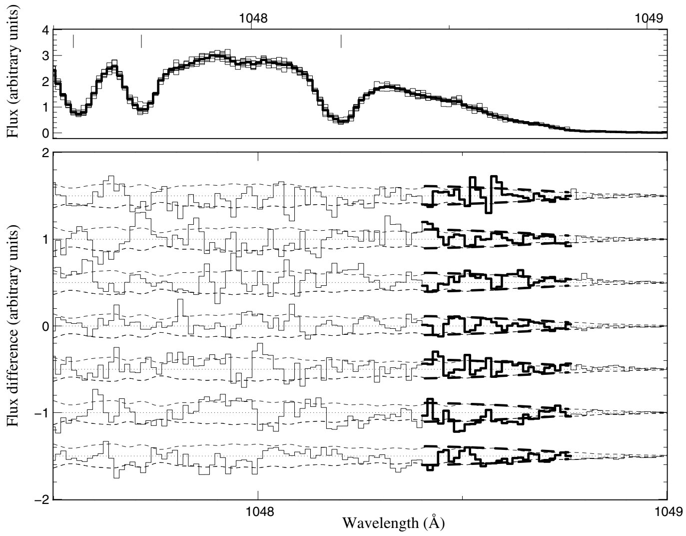

Fig. 13. FUSE LWRS HD 34078 spectra near the 1050 Å broad (4–0) H_2 Lyman band. *Upper panel*: all epochs, after flux intercalibration and alignment (see text). The mean spectrum is shown (thick line); tick marks indicate the features shown in Fig. 12 (two are from H_2, the third is from Ar I). *Lower panel*: difference between the spectrum for each epoch and the mean spectrum (epochs 1 to 7, shifted from top to bottom for clarity; same scale as in the upper panel). The dashed line shows the 3σ variance among the different epochs. The region used in the analysis is shown (thick line).

4. Variations in the H_2 column density

Boissé et al. (2005) analyzed the first 5 FUSE spectra taken since 2000 and detected no variation for the H_2 column density with an upper limit of 5% at a 3σ confidence level. Three additional spectra were obtained by FUSE in September 2003, February 2004 and October 2004 which allow us to follow the time behavior of H_2 absorption during the nearly five years since January 2000 and then probe the spatial distribution of the gas over scales up to 104 AU.

4.1. Contamination of HD 34078 spectra by nebular emission

Comparing the October 2004 (8th) spectrum to the previous ones, we find that it shows noticeable differences (Fig. 12): narrow lines are deeper and damped H_2 lines are slightly broader [as if $N(H_2)$ had increased]. This brought to our attention a potential difficulty that had not been considered in B05: contamination of the HD 34078 spectrum by diffuse emission from the IC 405 nebula. Indeed, the 8th spectrum was obtained with the MDRS aperture while all others were taken using the larger LWRS aperture. Given the difference in size (MDRS: 4×20 arcsec^2; LWRS: 30×30 arcsec^2) and the intense diffuse emission detected close to the HD 34078 line of sight by France et al. (2004), the peculiarities of the 8th spectrum might just be due to a lower level of contamination of the spectrum by diffuse emission. In Appendix A, we estimate the nebular contribution to LWRS spectra and conclude that it can explain the difference between FUSE spectra 1 to 7 and the 8th MDRS one. Thus only spectra 1 to 7 will be considered below in our search for variations in H_2 lines.

The importance of diffuse emission contamination in LWRS spectra also implies some limitation in our search for variations: the aperture may not be located exactly at the same position on the sky at all epochs resulting in a slightly variable contribution from diffuse emission if gradients are present. Note that since the diffuse to stellar flux ratio decreases with wavelength towards HD 34078 (France et al. 2004), H_2 systems at longer wavelengths are best suited to minimize the contamination by diffuse emission. Regarding the study of the gas properties towards HD34078, the 8th spectrum is clearly to be preferred for two reasons: i) it should be much less affected by diffuse emission and ii) the S/N ratio is significantly higher than for previous spectra due to an integration time (22 500 s) about four times longer than at epochs 1 to 7 (≃6000 s). A redetermination of the gas properties based on the 8th spectrum (H_2 excitation diagram in particular) will be presented elsewhere; we simply note here that the detection of absorption lines from all excited H_2 levels quoted in B05 is confirmed.

4.2. Variations in N(H_2, J = 0)

As in B05, we perform a direct comparison of the LWRS spectra, after relative flux intercalibration and adjusment of the wavelength scale. This procedure is applied independently to three portions of the spectra located at about 1050, 1063 and 1078 Å, corresponding to the (4–0), (3–0), (2–0) H_2 Lyman bands respectively. Each of these broad features is a blend of four H_2 lines arising from the J = 0, 1 and 2 levels. A good relative flux calibration is easily obtained (as for spectra 1 to 5), indicating that the shape of the stellar spectrum does not vary (known stellar lines for such O9 stars are indeed weak and rare in these regions: Pellerin et al. 2002). Using narrow high J H_2 lines adjacent to the broad H_2 absorptions of interest, we get an accuracy in the wavelength alignment of about 0.01 Å for the 1050, 1063 and 1078 Å absorption systems.

We now focus on the blue edge of each broad H_2 system which presents good sensitivity to changes in $N(H_2, J = 0)$. A zoom of this region for the 1050 Å system is shown in Fig. 13 (upper panel). All spectra, corrected in flux and wavelength as described above, are superimposed. They are all similar and an average spectrum can therefore be computed (thick line). The difference (ΔI_i) between one individual spectrum, i, and the mean is displayed in the lower panel for each epoch ($i = 1, ..., 7$ from top to bottom). The 3σ dispersion on ΔI_i among the seven epochs is indicated as a function of wavelength (dashed lines). Away from the $J = 0$ line, the ΔI profile is consistent with no variation. In the region close to the $J = 0$ line (displayed in red) where variations in $N(J = 0)$ would induce changes in the profiles, spectra 1 to 7 are also consistent with the mean spectrum. Similarly, B05 have adjusted the first spectra using $\log N(J = 0) = 20.52$ and concluded that the variation among the five first spectra was lower than 5%. Indeed, an increase (decrease) of this amplitude roughly corresponds to a difference that follows the lower (upper) 3σ profile in Fig. 10. We conclude from our analysis that $N(H_2)$ changed by less than 5% at the 3σ level between January 2000 and February 2004 while N(CH) has undergone variations as large as 20% over the same time interval (cf. Fig. 6).

5. Observations summary

5.1. The stability of ζ Per CH absorption

As mentioned above, ζ Per was observed primarily to test the homogeneity of our measurements. After correction of the small offset found in the OHP/ELODIE data, the whole set of W values appears remarkably consistent. The latter, and the most recent (2006–2008) data in particular, lead us to a strong twofold conclusion: i) W_{4300}(CH) remains constant towards ζ Per and ii) N(CH) and N(CH$^+$) do vary towards HD 34078. Indeed, if variations of instrumental origin were responsible for changes in HD 34078 values, one should invoke a very unlikely "conspiracy" to explain the stability of ζ Per lines. The fact that the same behavior is observed for distinct CH$^+$ lines is a strong additional proof of the reality of HD 34078's variations.

ζ Per was observed for 5 years and over this time interval, the drift of the line of sight through the foreground cloud has been significant. The distance to the cloud is thought to be 350 pc (Hilton & Lahulla 1995) and thus the drift of the line of sight amounts to 17.8 AU. The constancy of N(CH) then shows that over this scale and below, there is no marked structure in the cloud. The 3σ upper limit on relative variations of N(CH) is about 6%. We derive this value simply from the raw average and rms scatter of McD and OHP/SOPHIE measurements, assuming the CH λ4300 line is optically thin; a more detailed analysis of the ζ Per data, including CN and CH$^+$ lines, will be presented elsewhere.

5.2. Main observational results on HD 34078

From multiwavelength observations of the gas towards HD 34078 and in its close environment, we obtain the following results:

- ⋆ the ^{12}CO(2–1) emission map of the HD 34078 field shows a pronounced peak coincident with the star's position, clearly indicating that molecular gas seen in absorption is closely associated with HD 34078. The extent and morphology of the CO emission correlates well with the 24 μm dust emission arc of France et al. (2007). Presumably as a result of the interaction between HD 34078 and the ambient cloud, the CO(2–1)/CO(1–0) ratio is anomalously large, pointing towards dense (10^3–10^4 cm^{-3}) and warm ($T > 12$ K) emitting gas and further, a remarkable kinematical pattern with doubled-peaked profiles is observed;
- ⋆ we confirm the reality of rapid, large amplitude (typically 10% yr^{-1}) and correlated variations of N(CH) and N(CH$^+$) towards HD 34078. The velocity ranges covered by CH and CH$^+$ narrow absorption coincide well with that of CO emission. Variations in CH and CH$^+$ line profiles are unambiguously detected; these occur mainly in the blue part of the narrow absorption. A broad shallow and relatively stable component is seen for both CH and CH$^+$ in the interval [–4, 17 km s^{-1}];
- ⋆ comparison of LWRS and MDRS FUSE spectra reveals that the 7 LWRS spectra available are significantly contaminated by diffuse light from IC 405. The absence of variations in the LWRS profiles of H_2 $J = 0$ lines yields a 3σ upper limit of 5% on N values, extending the result of B05 over nearly four years (or 90 AU).

6. Discussion

Given the marked contrast between the stability of ζ Per CH lines and the rapid, large amplitude variations seen for CH and CH$^+$ towards HD 34078, we shall assume in the following discussion that these variations can be attributed entirely to phenomena associated with the star/cloud interaction and not to small scale structure in cold gas.

6.1. Towards a coherent picture of the close environment of HD 34078

From the broad set of observations available, a coherent scenario emerges which can be summarized as follows. HD 34078 recently encountered a molecular cloud, as originally suggested by Herbig (1958). The stellar wind impacts the ambient material resulting in a shell of compressed, highly excited gas. Modelling of both the H_2 excitation (B05) and CO emission (Sect. 2.2) provides consistent estimates for the density in the shell, $n \simeq 10^4$ cm^{-3}. Dust grains located in this region are directly exposed to the intense UV flux from the O star and strongly emit at infrared wavelengths. Thus, both the mid-IR emission detected by France et al. (2007) and the CO emission probably delineate the part of the shell seen edge-on by the observer, accounting for the good correlation between the *Spitzer* 8 or 24 μm arc and the CO map (Fig. 1).

B05 favored a two-cloud model on the basis of the dichotomy in the physical conditions derived for the highly excited H_2 on the one hand and for all other molecular absorption on the other hand. They discarded a single cloud model (although it would have naturally explained the similar velocity for all absorption lines and the presence of preexisting diffuse H_2 near HD 34078 ...) because they implicitly assumed that molecules should be photodissociated at the very small distance (a few 0.01 pc) implied by the modelling of the H_2 excitation. In fact, this argument is valid only in a model that is stationary regarding the formation/destruction of molecules. Given the large space velocity (V_s) of HD 34078, its arrival is so recent that probably no such steady-state equilibrium could be established. Rather, as the O star is approaching the cloud, a photoionisation and photodissociation front develops, moving at velocities of the order of a few km s^{-1} only (Bertoldi & Draine 1996), i.e. well below the star velocity. The distance between HD 34078 and these fronts then gradually decreases and the velocity of the latter becomes higher (the front velocities increase with stellar flux), up to a point where the star and front velocities equate.

Moreover, the stellar wind has a strong mechanical impact on the surrounding gas and the latter is gradually set into motion

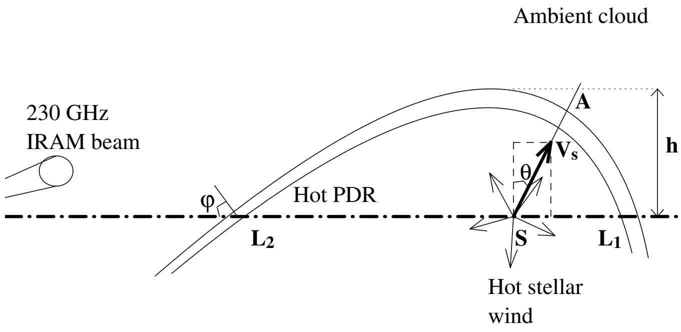

Fig. 14. Geometrical parameters associated with the bow shock around HD 34078 (h is the apparent standoff distance; $h \simeq 0.04$ pc). The velocity vector V_s shown as the bold arrow is inclined by $\theta = 30°$ with respect to the plane of the sky. "S" marks the star position while the dot-dashed horizontal line represents the line of sight to the star (the observer being on the left). The double curve is the projection of the proposed bow shock. Optical and UV spectra of HD 34078 probe the bow shock/hot PDR at L_2 (with an inclination angle φ; we estimate $SL_2 \simeq 0.1$ pc) and the foreground ambient cloud while IRAM 230 GHz observations involve all material enclosed into the beam.

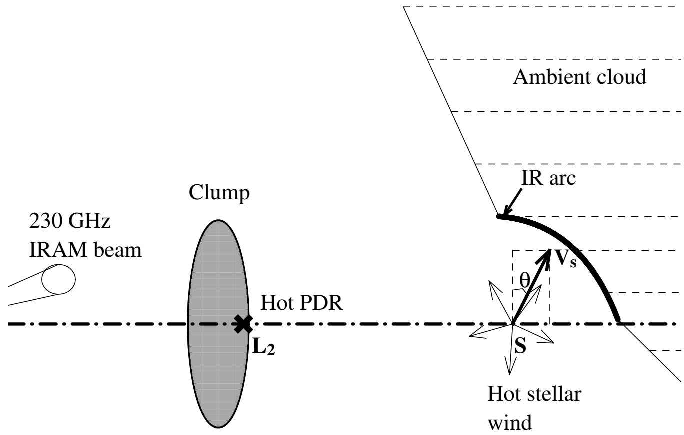

Fig. 15. Alternative scenario to the one presented in Fig. 14. Here, HD 34078's wind slightly modifies the shape of the ambient cloud boundary, giving rise to the IR arc. The clump reddens the star but not the surrounding nebular emission; further, gas located on its cold side (facing the observer) induces narrow absorption in the ^{12}CO(2–1) emission profiles as well as some visible and UV absorption lines. Excited H_2 lines and a significant fraction of CH and CH^+ absorption originates from the PDR located on the hot side of the clump, intersected by the line of sight at L_2.

as a result of momentum flux. When the star is close enough to the cloud, a stationary bow shock is established at a position nearly coincident with that of the photodissociation front. At this stage, the distance ($R_0 = AS$, see Fig. 14) between the star and the apex of the shock is well defined and remains constant as long as the density of the ambient cloud and the wind properties (mass loss rate and terminal velocity) do not change. In this picture (Fig. 14), whether the dynamical steady-state regime is established or not, the molecular material located beyond the front/shock surface should be little affected by the presence of the closeby star, thereby accounting for the characteristics of the molecular components that B05 assigned to the "translucent" component.

We conclude that a model involving a single cloud located very close to HD 34078 may, in fact, be consistent with all observations. A key issue remains open however: at what stage of the star-cloud interaction have we captured HD 34078 and its close environment? A stationary dynamical regime is expected to be established ultimately and in the thin-shell limit, detailed models describing the geometry and velocity structure of steady-state bow shocks are available (e.g. van Buren et al. 1990; Mac Low et al. 1991; Wilkin 1996). We thus performed a detailed comparison between the predictions of these models and observations (Appendix B). From this analysis, we conclude that the IR/CO arc does not display the properties expected for a stationary bow shock and that we are possibly observing a "nascent bow shock", i.e. the wind/cloud interaction at an early evolutionary stage, well before the formation of a steady-state flow around the star. We also find that the geometrical constraints provided by the IR data, $h \simeq R_0 \simeq 0.04$ pc, are roughly consistent with the radiation field implied by the modelling of H_2 excitation (B05).

A variant of the above scenario is suggested by France et al. (2004), who proposed that differential extinction is present between HD 34078 and the surrounding diffuse emission, in order to explain the increase of the diffuse to stellar ratio at far-UV wavelengths. More specifically, France et al. (2004) propose that a small clump lies in front of HD 34078 (Fig. 15). With an extent no larger that about 20″, the latter could induce the observed HD 34078 extinction without affecting the surrounding nebular emission.

Such a picture is attractive in our context because 20″ is approximately the size of the area over which a "dip" is seen in the CO profiles, suggesting that the double-peaked line shapes might be due to narrow absorption rather than to velocity structure in the emitting gas. In this scenario, CO emission could originate from the ambient cloud background to HD 34078 – especially its outer boundary, compressed by the wind – accounting for the widespread emission seen over most of the field (Fig. 15). Additional emission could come from the clump itself, in particular from the region located immediately beyond the hot PDR facing the star, explaining the enhanced emission close to HD 34078 and the high excitation of the emitting material. Gas located on the cold side of the clump facing the observer should be little affected by the interaction, as in the bow-shock scenario. This region corresponds to the translucent component in B05's model; with a small CO excitation temperature and low velocity dispersion, this gas could induce narrow absorption in the background CO emission. The close similarity of the CO dip velocity at the star position, $V \simeq 6.0$ km s^{-1} (this value is stable to within 0.2 km s^{-1} among spectra displaying the dip), and the velocity of maximum narrow CH and CH^+ absorption (see Fig. 10) is consistent with absorption being responsible for the dip in CO profiles. The clump should be located at a distance from the star of about 0.1 pc (comparable to that of point L_2 in the bow-shock picture) so that the hot PDR facing the star is exposed to a radiation field large enough to account for the H_2 excitation (Appendix B, B05). In fact, the bow-shock and clump scenario are more or less equivalent, both of them involving the presence along the line of sight of a shell of dense gas illuminated by intense UV radiation; the main difference is that in the clump picture, the ambient material is not distributed in a continuous manner around HD 34078.

6.2. CH and CH^+ abundance and time variations

In the picture described above (Fig. 14), the dense shell at the wind/cloud interface is nearly static in the ambient cloud's frame and as time elapses, the point (L_2) at which the line of sight intersects the shell drifts over the latter towards the apex (A) at a velocity $V_t/\cos\varphi$, where V_t is the transverse velocity and φ is the inclination of the shell at L_2. Similarly, in the clump scenario (Fig. 15), the line of sight drifts over the wind/clump interface. The rapid CH and CH$^+$ variations observed imply that a significant fraction of these species is enclosed in a very localised region (with a size of about 10 AU, corresponding to a time interval of 6 months) and in our context, it is natural to assume that time variations arise from structure over the shell of compressed gas intersected by the line of sight. Further, as already outlined by B05, the CH/H$_2$ ratio towards HD 34078 is anomalously large: for N(CH) $\simeq 10^{14}$ cm^{-2} (the largest values reached, in 2000–2003) we get a ratio of 1.6×10^{-7}, which appears to be 3.7 times larger than the value inferred from the best fit given by Sheffer et al. (2008) (a similar result is obtained by comparing HD 34078 values to those compiled by Welty et al. 2006). Since the CH–H$_2$ correlation is quite good, such a deviation is very significant and indeed, in Fig. 8 presented by Sheffer et al. (2008), HD 34078 is clearly an outlier (note that surprisingly, HD 37903, the other star showing highly excited H$_2$, has an anomalously *low* CH/H$_2$ ratio). The CH$^+$/H$_2$ ratio displays much more scatter among all sightlines, but nevertheless, N(CH$^+$) towards HD 34078 is among the largest values for N(H$_2$) $\simeq 6 \times 10^{20}$ cm^{-2} (Fig. 10 in Sheffer et al. 2008). In the end, the CH/CH$^+$ ratio in HD 34078 is well within the range observed towards other stars (cf. Fig. 10 in Welty et al. 2006). We thus apparently have a comparable relative excess of both CH and CH$^+$, and again, it is natural to assume that the overproduction of these species occurs in the compressed shell. To induce such a large deviation in the CH/H$_2$ ratio, the overproduction of CH must be quite large since molecular gas located beyond the shell probably displays a more standard ratio. Similarly, the spatial distribution of CH and CH$^+$ over the shell must be very inhomogeneous at scales of about 10 AU to induce the observed variations. Since the CH and CH$^+$ variations are strongly correlated, a single mechanism must be at work to explain the overproduction of both species.

Clearly, the CH and CH$^+$ time variations cannot be attributed to pure density structure. Indeed, no corresponding changes have been seen for N(H$_2$) and further, explaining CH or CH$^+$ variations by more or less spherical clumps with a size of about 10 AU would require very high volumic densities, n(H$_2$) $\simeq 10^{5-6}$ cm^{-3}, as argued by R03. In such gas, CH$^+$ would be rapidly destroyed by reactions with H$_2$. Then, the structure is likely to be more *chemical* in nature.

The production of CH$^+$, which is not expected at thermal equilibrium, together with the correlated variations of CH and CH$^+$, suggest that both molecules are mainly formed in the dense shell, through a MHD shock where the drift velocity between ions and neutrals triggers the formation of both CH$^+$ and CH (Pineau des Forêts et al. 1986; Flower & Pineau des Forêts 1998). CH$^+$ could also be overproduced at the interface between the ambient cloud and warmer gas, as suggested by Duley et al. (1992), Crawford (1995) and more recently by Lesaffre et al. (2007). In the specific conditions prevailing around HD 34078, one may imagine that Rayleigh-Taylor instabilities develop efficiently (e.g. as a result of fluctuations in the wind properties or in the ambient cloud), leading to the formation of a turbulent mixing layer with pronounced small-scale structure. HD 34078 being variable (Marchenko et al. 1998), stellar flux variations can also trigger or amplify the formation of small-scale structure at the interface and in the PDR. In regions hot enough to form significant amounts of CH$^+$ via the endoenergetic C$^+$ + H$_2$ reaction (whatever the heating mechanism, shocks or turbulent dissipation), small spatial temperature fluctuations will result in appreciable variations in the CH$^+$ formation rate and then in the relative abundance of CH$^+$ and CH (recall that CH is easily formed from CH$^+$ once the latter species is present). One can indeed estimate that since the CH$^+$ formation rate scales as $\exp(-4640/T)$, a local variation as small as 22 K around $T \simeq 1000$ K is sufficient to induce a fluctuation of 10% in the local abundance. The broad, shallow CH and CH$^+$ absorption components (Fig. 10) could be a signature of the highly turbulent velocity field at the interface (note the excellent agreement in the velocity intervals [–4 to 17 km s^{-1}] covered by the CH and CH$^+$ broad components, indicating that the species responsible for that component are cospatial).

CH and CH$^+$ line profiles vary mainly on their blue side, at $V_{\rm LSR} \simeq$ 4–5 km s^{-1}(Fig. 10), suggesting this velocity for the gas lying at the interface near L_2. This material is therefore blueshifted with respect to the ambient cloud (at $V_{\rm LSR} \simeq 6.5$ km s^{-1}); this is consistent with the stellar wind pushing ambient molecular gas towards the observer. The higher excitation derived for the CO component at $V_{\rm LSR} \simeq 5$ km s^{-1} also nicely fits this view. Thus, the scenario described above might, at the same time, explain in a coherent way the high abundances of CH and CH$^+$ as well as their time variations.

The amounts of excited H$_2$ (J = 3 to 5) and CH$^+$ are known to correlate (Lambert & Danks 1986) and is taken as an indication that the same mechanism is responsible for these species, the production of which requires an input of additional energy of yet unknown nature. Towards HD 34078, a marked excess of both excited H$_2$ and CH$^+$ is observed, in agreement with the correlation seen among more standard lines of sight. We note that in our scenario, the large amount of excited H$_2$ and CH$^+$ is a direct consequence of the proximity of HD 34078, through its wind and UV flux.

6.3. Small scale structure in quiescent H$_2$ gas

In the picture that we propose, H$_2$ gas located beyond the photodissociation front and shocked region is essentially unaffected by the presence of the star (dust grains should be somewhat warmer due to the proximity of the star, but at densities of a few 10^2 cm^{-3}, this has little impact on the gas temperature). This part of the cloud gives by far the dominant contribution to the H$_2$ column density in the J = 0 level (in B05's model, the hot PDR represents less than 1% of the total N value); it should also contain a significant fraction of the CO responsible for the UV absorption, about 1/4 of CH molecules (cf above) and most of the CN. Thus, the lack of variation in N(H$_2$, J = 0) at a level better than 5% implies that no marked small-scale *density* structure is present within the fraction of the ambient cloud probed by the drift of the line of sight between 2000 and 2004. If this region is representative of quiescent diffuse molecular material in general, the structure seen elsewhere for other tracers like H$_2$CO, HCO$^+$, and OH would be mainly "chemical" structure, possibly reflecting the specific formation/destruction processes relevant to these species.

We further note that the lack of structure in quiescent H$_2$ gas is consistent with the stability of CH absorption lines towards ζ Per, provided the CH/H$_2$ abundance ratio is uniform at scales of about 10 AU within this quiescent cloud.

7. Conclusions and prospects

- By mapping ^{12}CO(2–1) emission around HD 34078, we have unambiguously shown that the molecular material seen in the foreground is closely associated with the star, supporting the suggestion by Herbig (1958) that HD 34078 is currently encountering a molecular cloud. Repeated CH and CH^+ observations, performed using the star ζ Per as reference, confirm the reality of rapid and large amplitude variations of N(CH) and $N(CH^+)$ along the line of sight.

- The results altogether strongly suggest that the recent arrival of HD 34078 near the southern edge of a molecular cloud has given rise to a shell of dense gas at the interface between the stellar wind and H_2 gas, the latter material belonging either to the distorted boundary of the ambient cloud or to a small foreground clump, as suggested by France et al. (2004). The location of this shell relative to the star is consistent with constraints derived from earlier modelling of H_2 excitation. By comparing the geometrical characteristics of the IR arc detected by France et al. (2007) and the velocity field inferred from our CO or optical observations to predictions of steady-state bow shock models, we find that the latter are inconsistent with the observed properties. Therefore, we may be seeing this region at an early phase of the wind/cloud interaction, with a dense layer formed at the interface but no stationary flow yet established.
- We propose that the large relative CH and CH^+ abundances originate from significant overproduction of CH^+ in the dense shell, due to the presence of a strong C-shock and/or of mixing of warm ionised gas and highly excited molecular material at the wind/cloud interface. The pronounced, correlated CH and CH^+ variations would then reflect marked chemical structure in the dense shell, possibly resulting from instabilities occuring at the interface.
- No variations of $N(H_2, J = 0)$ have been found at a level of 5% (3σ limit), extending the result obtained in B05 to a time interval of 4 years, or 110 AU. In the scenario that we propose, $J = 0$ H_2 molecules are mainly located beyond the dense shell. This indicates that beyond the photodissociation and photoionisation fronts, where the molecular material is not yet affected by the interaction with HD 34078, no marked small-scale scale structure is present and that the bulk of the mass is distributed relatively uniformly within the cloud.

Let us now discuss some prospects concerning the time evolution of HD 34078's environment, assuming the scenario sketched in this paper is roughly correct. One may in particular wonder whether the future evolution can induce significant observable changes in the coming years. Using the estimates for the observed standoff distance and its expected steady-state value given in Appendix B, one can get a lower limit for the time needed for a stationary flow to establish, $(R_{0,\rm obs} - R_{0,\rm th})/V_{\rm s} \simeq R_{0,\rm obs}/V_{\rm s} \simeq 350$ yr. We therefore expect very little change in the morphology of the mid-IR or CO emission. The only appreciable evolution would involve the motion of the star relative to the IR or CO peak (1″ in 23 yrs), since the shell is supposed to remain nearly static in the near future.

However, during its evolution towards a stationary dynamical regime, the velocity field must undergo a drastic variation to reach the steady-state solution. CO mm observations, which provide excellent spectral resolution, might thus reveal significant velocity changes. A higher spatial resolution map of CO emission would be useful in this regard and of great help to better understand the kinematics underlying the remarkable pattern observed for line profiles in Fig. 1. In the next decade, ALMA will offer excellent opportunities for such observations. Numerical simulations of the time evolution of the wind/cloud interface (which, to our knowledge are not available) would also be very useful to indicate how the evolution of the velocity field will proceed in the early phase.

In the above reasoning, we implicitly assumed that the dense shell will smoothly evolve towards the steady-state solution but this is in no way evident. If indeed instabilities develop efficiently at the interface (as suggested by CH and CH^+ variations), the cloud may simply be gradually destroyed as the star moves. Such a picture would be consistent with the suggestion by Herbig (1958) that the absence of IS material south of the star is due to "clearing" along the path followed by HD 34078 in the past (the clump involved in the second scenario might then simply be a fragment of the initial cloud in the process of photoevaporation).

Focusing now on the present state of HD 34078's environment, we note that it represents a remarkable PDR and shock for which many observational constraints are or might be available, thanks to the presence of a background UV-bright star. Geometrical parameters are now well determined and physical conditions in the ambient cloud relatively well constrained (sensitive CO emission observations further away from HD 34078 would allow us to better characterize them and verify that the peculiar excitation conditions determined in Sect. 2.2 are specific to the immediate vicinity of the star). Then, the HD 34078 PDR may be used as a reference to test our understanding of various physical and chemical processes occuring elsewhere at cloud interfaces subject to less extreme conditions.

Acknowledgements. We warmly thank observers at OHP and S. Ilovaisky in particular for spectra taken there with ELODIE and SOPHIE as well as J. Krelowski, G. Galazutdinov, F. Musaev and A. Bondar for collecting the Terskol, BOAO and Calar Alto spectra. We are also indebted to M. Gerin and L. Pagani for their assistance in the preparation of IRAM observations, to J. M. Désert for help in the FUSE data reduction, and to K. France for providing the *Spitzer* 24 μm map. Finally, we are grateful to S. Cabrit, F. Martins and J. Zorec for several helpful discussions. Part of this work was supported by the french INSU National Program PCMI (Physique et Chimie du Milieu Interstellaire).

Appendix A: The contribution of the IC 405 nebula to HD 34078 spectra

France et al. (2004) observed the diffuse emission from IC 405 at four positions (their Pos1 to Pos4), two of which (Pos1 and Pos2) are located close to the HD 34078 position (75″ offset, E and W respectively). Thus, diffuse emission is certainly present towards HD 34078 itself and may contribute significantly to the flux collected in the FUSE apertures. To estimate this contribution, we retrieved from the FUSE database the spectra obtained at Pos1 to Pos4 (cf. Fig. 1 from France et al. 2004). Pos2 is the brightest region; around 1050 Å, the surface brightness is about 30% larger than at Pos1, indicating spatial variations of this emission. Since Pos1 and Pos2 are symetrically located with respect to HD 34078, a first order estimate of the diffuse flux towards the star is the average of Pos1 and Pos2 spectra. We thus estimate that the diffuse flux received in the LWRS aperture is about 7% of the HD 34078 flux around $\lambda = 1050$ Å (this fraction decreases with wavelength since the diffuse to stellar flux ratio gets lower at longer wavelengths, as discussed by France et al. 2004). If the surface brightness is locally uniform over the LWRS aperture centred on HD 34078's position, the contribution of diffuse emission scales linearly with aperture size and should be about 11 times lower in MDRS spectra. Thus, while LWRS spectra of HD 34078 are significantly affected by diffuse emission, the MDRS spectrum should be essentially free of such "pollution", except possibly at the shortest wavelengths.

To estimate the impact on HD 34078's LWRS spectra of the contamination by diffuse emission, one needs to examine the spectrum of the latter (the Pos1 spectrum is displayed in Fig. 7 from France et al. 2004). Although its S/N ratio is limited, it is clear that it differs from that of HD 34078 in two respects. First, narrow lines appear to be fainter and shallower (only the strongest lines are detected); this is due, at least in part, to the lower effective resolution implied by the extented nature of the source. Second, broad H_2 lines are narrower, indicating that the average pathlength of scattered photons through the molecular gas is shorter than that followed by direct HD 34078 photons. These two properties of diffuse emission qualitatively explain the peculiarities of the 8th spectrum and indeed, one finds that by combining it and our estimate of the diffuse emission spectrum towards HD 34078, it is possible to reproduce spectra 1 to 7 fairly well. We conclude that the apparent changes in the 8th spectrum can be attributed mainly to a smaller contribution of diffuse emission due to the use of MRDS instead of LWRS in the earlier spectra.

Appendix B: The steady-state bow shock model compared to observations

Extensive work has been performed to describe the geometry and velocity structure of steady-state bow shocks (e.g. van Buren et al. 1990; Mac Low et al. 1991; Wilkin 1996) and in the thin-shell limit, there are simple analytical predictions that can be directly compared to observations.

B.1. Shape and radius of the shell

Assuming that the IR arc detected by France et al. (2007) corresponds to a steady-state bow shock viewed in projection onto the sky, we can first check whether the apparent geometrical properties are consistent with the predicted ones. At first sight, the distance between the star and the apex of the bow shock looks too small compared to its radius of curvature on the *Spitzer* image but we have to account for projection effects which somewhat influence the appearence of the arc. HD 34078's tangential and radial components (V_t and V_r respectively) are well constrained by observations; we adopt $V_t = 100\,\mathrm{km\,s^{-1}}$ and $V_r = +59\,\mathrm{km\,s^{-1}}$ (in the LSR system; we remeasured the latter value from our own visible spectra). The velocity vector is then inclined by an angle $\theta = 30°$ with respect to the plane of the sky (Fig. 14).

To estimate the impact of projection effects on the $h/R_{c,p}$ ratio, where h is the apparent standoff distance ($h/D \simeq$ 10–20″ after France et al. 2007, we adopt $h/D = 15''$ with $D = 530$ pc, the distance to HD 34078) and $R_{c,p}$ is the radius of curvature of the arc as seen in projection on the sky ($R_{c,p}/D \simeq 37''$), we approximate the bow shock geometry by a paraboloid (van Buren et al. 1990; Wilkin 1996) and find after some algebra that

$$h = \frac{3+\cos^2\theta}{4\cos\theta} R_0 \tag{B.1}$$

and

$$R_{c,p} = \frac{3}{2\cos\theta} R_0, \tag{B.2}$$

where R_0 is the distance between the star (S) and the apex (A) of the shock. With $\theta = 30°$, we get $h = 1.08 R_0$ and $h/R_{c,p} = 0.62$ while the estimate inferred from the IR map is $h/R_{c,p} = 0.40$ (the upper limit is 0.54 for $h = 20''$). Thus, projection effects appear to be insufficient to explain the relatively large radius of curvature of the arc. Moreover, it seems difficult to explain in this model why the arc does not extend further southward (cf. Fig. 5 in France et al. 2007). Given that projection effects are in the end very limited, the standoff distance can be estimated to be about 0.04 pc.

Although the observed arc shape is not well fitted by the model prediction, the IR data can nevertheless be used to get a rough estimate of the distance between the star and the point where the line of sight intersects the shell (L_2 in Fig. 14), by making the reasonable assumption that the latter is axially symmetric. From the 24 μm map, we estimate that $d(S, L_2)/D \simeq 40''$, implying $d = 0.10$ pc. Is this value compatible with the UV flux necessary to explain the amount of highly excited H_2? B05 found that a radiation field about 10^4 larger than that in the local ISM is required, which is obtained at 0.2 pc from the HD 34078, a value in reasonable agreement with our estimate for $d(S, L_2)$.

B.2. Momentum balance and ambient density

In steady-state, the standoff distance, R_0, is set by a momentum balance equation (Eq. (2) in van Buren et al. 1990; Eq. (1) in Wilkin 1996) which is

$$R_0 = \sqrt{\frac{\dot{m}_\star V_w}{4\pi\rho_a V_\star^2}} \tag{B.3}$$

where $\dot{m}_\star$ is the mass loss rate, V_w the terminal wind velocity ($10^{-9.5}\,M_\odot\,\mathrm{yr^{-1}}$ and 800 km s^{-1} respectively after Martins et al. 2005), ρ_a the mass density of the ambient medium and V_s the star velocity (116 km s^{-1} with the above values for V_t and V_r). The ambient H number density can be estimated either from C I$^{(*,**)}$ ($n = 700\,\mathrm{cm^{-3}}$; B05) or C_2 absorption lines ($n = 300\,\mathrm{cm^{-3}}$; Federman et al. 1994), assuming the latter are not significantly contaminated by the dense shell. Adopting $n = 500\,\mathrm{cm^{-3}}$, we get a "theoretical" value of $R_0 = 3.5\times10^{-4}$ pc while observations indicate $R_0 \simeq 0.04$ pc, in marked disagreement. In other words, an ambient density as low as of a few $10^{-2}\,\mathrm{cm^{-3}}$ would be required for a steady-state bow shock to be at the observed distance, which is highly unrealistic for molecule-rich gas. Radiative pressure from stellar photons might help to maintain the shell at a distance larger than expected on the basis of the wind pressure alone. One can obtain easily an upper limit for the radiative to wind pressure ratio, P_{rad}/P_w, by assuming that all photons impinging on the shell are absorbed: $P_{rad}/P_w = L/(\dot{m}_\star c V_w)$. This ratio is of the order of 10^{-3} for HD 34078; radiation pressure is therefore negligible here.

Since P_w scales linearly with $\dot{m}_\star$, one may wonder whether the mass loss rate has been underestimated. Prior to the study by Martins et al. (2005), the adopted value for HD 34078 was $10^{-6.6}\,M_\odot\,\mathrm{yr^{-1}}$ (i.e. larger by a factor of 800 than the present estimate) and even with this much higher rate, the required ambient density would amount only to $n \simeq 20\,\mathrm{cm^{-3}}$. The much lower recent mass loss estimate is based on the availability of UV lines (C IV λ1550 mainly) which better probe weak winds; the uncertainty on the revised value is estimated to be of a factor of about 3 (F. Martins; private communication). Then, $\dot{m}_\star$ cannot have been underestimated by a factor large enough to explain the discrepancy between the observed and theoretical steady-state R_0 values.

Stationary bow shock models also provide specific predictions for the mass surface density or equivalently the column density N(H) of swept-up material trapped in the bow shock (cf. Eq. (7) from van Buren et al. 1990; or Eq. (12) from Wilkin 1996). N(H) scales as $\dot{m}_\star^{1/2} V_W^{1/2} V_S^{-1} n^{1/2}$ and with the values quoted above, we get $N(\mathrm{H}) = 6.0\times10^{17}\,\mathrm{cm^{-2}}$. This prediction is to be compared to the H column density in the hot PDR component of B05: 2.7×10^{19} cm^{-2}, including H_2 only (their Table 4). Note that their exceedingly large predicted value for the H I column density was due to the assumption of steady-state equilibrium for the photodissociation of H_2; in our scenario, this assumption is no longer realistic. The observed value corresponds to the dense material along the line of sight to HD 34078 (i.e. located at L_2 in Fig. 14) while the "theoretical" one refers to the apex position (A in Fig. 14). This does not make a large difference however since Wilkin's results (his Fig. 4) indicate that the surface density normal to the bow shock varies slowly with position away from the apex. One should also consider that in the geometry of Fig. 14, the shell is not crossed normally by the line of sight but with an inclication angle φ, but this involves a factor of at most a few. Obviously, this cannot explain the large discrepancy between the two values above.

In the 24 μm map, the arc defines a roughly hemispherical cavity (with a radius of about $R_{\rm c,p}$) and one can easily get another estimate for the column density in the compressed shell by simply assuming that material from the ambient cloud (i.e. with $n = 500$ cm^{-3}) initially filling this cavity has been swept by the stellar wind to form the present shell. This leads to a column density of $N = nR_{\rm c,p}/3$ and interestingly, this expression provides a value, $N \simeq 5 \times 10^{19}$ cm^{-2}, comparable to the estimate of B05 for the hot PDR component.

B.3. Velocity field of the compressed gas

Another way to assess whether a steady-state bow-shock model is consistent with our data is to compare the observed and predicted velocity fields. Since ^{12}CO(2–1) emission traces dense gas within the shell of compressed gas, our CO data can be used to constrain the velocity field around HD 34078. One may wonder in particular, whether the double-peaked profiles with their remarkable symmetry properties (Fig. 1) simply arise from the fact that the IRAM beam intersects the paraboloidal wind/cloud interface twice. To compute a "synthetic" ^{12}CO(2–1) emission map, we adapted the model developed by Pety et al. (2006) to describe the outflow around HH30. We relied on the analytical expressions provided by Wilkin (1996) for the geometry, velocity field and mass surface density (see also van Buren & Mac Low 1992), with the parameter values considered above. For practical reasons, the thickness of the boundary layer has been assumed to be $R_0/20$ (while it is zero in Wilkin's model) and the absolute surface mass density has been scaled so as to reproduce the observed intensity. The underlying assumption is that the medium is optically thin which is reasonable given the strength of the CO emission. The resulting signal model was convolved with the IRAM-30 m 230 GHz beam, an important step given the beam size relative to the source extent. Finally, in order to assess whether a specific model is acceptable or not, we compared the synthetized and observed maps of spectra as well as position-velocity and channel maps.

Several difficulties arised when comparing the model to observations. First, the extent of the ^{12}CO(2–1) emission tends to be too limited if one adopts $R_0/D = 15$ arcsec. This is related to the fact that the expected radius of curvature is too small for such a R_0 value, as compared to the observed one (cf. above). Since here we are mainly interested in the velocity field, we simply adjusted R_0 so as to match the observed extent of the emission. Second, the velocity range over which ^{12}CO(2–1) emission appears in the model is much larger than the observed one. Indeed, the velocity field of the gas scales linearly with $V_{\rm s}$: in particular, the typical separation ΔV between the two CO emission peaks near HD 34078's position should be of the order of 0.7 $V_{\rm s}$ while we observe only 0.02 $V_{\rm s}$ (corresponding to about 2 km s^{-1}). Artificially modifying the star's velocity to the former value allows us to qualitatively reproduce the emission properties close to the star. However, the double-peaked character of the model profiles tend to be less pronounced that in the observed ones. Other velocity/density distributions might be considered to get a better fit, but clearly, only higher spatial resolution observations would allow us to obtain unambiguous constraints on such models.

Another constraint can be obtained from optical absorption lines arising towards HD 34078. With the parameters quoted above, the expected velocity of the gas from the shell along the sightline to HD 34078 (i.e. at L_2) is $V_{\rm LSR} \simeq -15$ km s^{-1}. Such a shift between highly excited H_2 lines (tracing the dense layer) and absorption from species located beyond the shell would be easily detectable, but B05 failed to find any significant velocity difference between the two components.

To summarize, the dense shell at the stellar wind/molecular cloud interface (with a density of about $n \simeq 10^4$ cm^{-3} and column density N(H) $\simeq 3 \times 10^{19}$ cm^{-2}, thus corresponding to a thickness of $\simeq 10^{-3}$ pc) is located at a distance of the star that is consistent with the excitation of H_2 but it does not display the properties expected for a steady-state bow shock: i) the arc is not curved enough; ii) the shell is too far from the star for the momentum balance to be satisfied; iii) the amount of material swept up by the wind is too large and iv) the velocity field shows very little deviation from the ambient value. The limited extent and somewhat irregular geometry of the arc are additional indications against a steady-state bow shock.

References

Allen, M. M. 1994, ApJ, 424, 754
Baranne, A., Queloz, D., Mayor, M., et al. 1996, A&AS, 119, 373
Bertoldi, F., & Draine, B. T. 1996, ApJ, 458, 222
Boissé, P., Le Petit, F., Rollinde, E., et al. 2005, A&A, 429, 509 (BO5)
Bouchy, F., & The Sophie Team. 2006, in Tenth Anniversary of 51 Peg-b: Status of and prospects for hot Jupiter studies, ed. L. Arnold, F. Bouchy, & C. Moutou, 319
Crane, P., Hegyi, D. J., & Lambert, D. L. 1991, ApJ, 378, 181
Crane, P., Lambert, D. L., & Sheffer, Y. 1995, ApJS, 99, 107
Crawford, I. A. 1995, MNRAS, 277, 458
Crawford, I. A. 2003, Ap&SS, 285, 661
Deshpande, A. A. 2007, in SINS – Small Ionized and Neutral Structures in the Diffuse Interstellar Medium, ed. M. Haverkorn & W. M. Goss, ASP Conf. Ser., 365, 105
Duley, W. W., Hartquist, T. W., Sternberg, A., Wagenblast, R., & Williams, D. A. 1992, MNRAS, 255, 463
Falgarone, E., Panis, J.-F., Heithausen, A., et al. 1998, A&A, 331, 669
Federman, S. R., Strom, C. J., Lambert, D. L., et al. 1994, ApJ, 424, 772
Flower, D. R., & Pineau des Forêts, G. 1998, MNRAS, 297, 1182
Frail, D. A., Weisberg, J. M., Cordes, J. M., & Mathers, C. 1994, ApJ, 436, 144
France, K., McCandliss, S. R., Burgh, E. B., & Feldman, P. D. 2004, ApJ, 616, 257
France, K., McCandliss, S. R., & Lupu, R. E. 2007, ApJ, 655, 920
Galazutdinov, G. A., Han, I., & Krełowski, J. 2005, ApJ, 629, 299
Heiles, C. 1997, ApJ, 481, 193
Herbig, G. H. 1958, PASP, 70, 468
Hilton, J., & Lahulla, J. F. 1995, A&AS, 113, 325
Hily-Blant, P., & Falgarone, E. 2007, A&A, 469, 173
Hoogerwerf, R., de Bruijne, J. H. J., & de Zeeuw, P. T. 2001, A&A, 365, 49
Lambert, D. L., & Danks, A. C. 1986, ApJ, 303, 401
Lauroesch, J. T. 2007, in SINS – Small Ionized and Neutral Structures in the Diffuse Interstellar Medium, ed. M. Haverkorn & W. M. Goss, ASP Conf. Ser., 365, 40
Lesaffre, P., Gerin, M., & Hennebelle, P. 2007, A&A, 469, 949
Lien, D. J. 1984, ApJ, 284, 578
Liszt, H., & Lucas, R. 2000, A&A, 355, 333

Liszt, H. S., & Lucas, R. 1998, A&A, 339, 561
Mac Low, M.-M., van Buren, D., Wood, D. O. S., & Churchwell, E. 1991, ApJ, 369, 395
Marchenko, S. V., Moffat, A. F. J., van der Hucht, K. A., et al. 1998, A&A, 331, 1022
Martins, F., Schaerer, D., Hillier, D. J., et al. 2005, A&A, 441, 735
McLachlan, A., & Nandy, K. 1984, MNRAS, 207, 355
Meyer, D. M., Lauroesch, J. T., Sofia, U. J., Draine, B. T., & Bertoldi, F. 2001, ApJ, 553, L59
Moore, E. M., & Marscher, A. P. 1995, ApJ, 452, 671
Pellerin, A., Fullerton, A. W., Robert, C., et al. 2002, ApJS, 143, 159
Pety, J., Gueth, F., Guilloteau, S., & Dutrey, A. 2006, A&A, 458, 841
Pety, J., Lucas, R., & Liszt, H. S. 2008, ArXiv e-prints, 808
Pfeiffer, M. J., Frank, C., Baumueller, D., Fuhrmann, K., & Gehren, T. 1998, A&AS, 130, 381
Pichon, C., Vergely, J. L., Rollinde, E., Colombi, S., & Petitjean, P. 2001, MNRAS, 326, 597
Pineau des Forêts, G., Flower, D. R., Hartquist, T. W., & Dalgarno, A. 1986, MNRAS, 220, 801
Rollinde, E., Boissé, P., Federman, S. R., & Pan, K. 2003, A&A, 401, 215 (R03)
Schuster, K.-F., Boucher, C., Brunswig, W., et al. 2004, A&A, 423, 1171
Sheffer, Y., Rogers, M., Federman, S. R., et al. 2008, ArXiv e-prints, 807
van Buren, D., & Mac Low, M.-M. 1992, ApJ, 394, 534
van Buren, D., Mac Low, M.-M., Wood, D. O. S., & Churchwell, E. 1990, ApJ, 353, 570
van Buren, D., Noriega-Crespo, A., & Dgani, R. 1995, AJ, 110, 2914
Weisberg, J. M., & Stanimirović, S. 2007, in SINS – Small Ionized and Neutral Structures in the Diffuse Interstellar Medium, ed. M. Haverkorn & W. M. Goss, ASP Conf. Ser., 365, 28
Welty, D. E. 2007, ApJ, 668, 1012
Welty, D. E., Federman, S. R., Gredel, R., Thorburn, J. A., & Lambert, D. L. 2006, ApJS, 165, 138
Welty, D. E., Simon, T., & Hobbs, L. M. 2008, MNRAS, 388, 323
Wilkin, F. P. 1996, ApJ, 459, L31